J. Fluid Mech. (2022), *vol*. 940, A29, doi:10.1017/jfm.2022.226

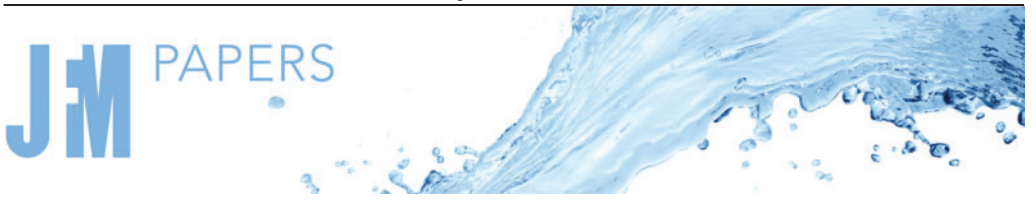

Mechanisms of the destabilized Mach reflection of inviscid oblique detonation waves before an expansion corner

Zijian Zhang[1], **Yunfeng Liu**[2,3] **and Chihyung Wen**[1,†]

[1]Department of Aeronautical and Aviation Engineering, The Hong Kong Polytechnic University, Kowloon, Hong Kong

[2]Institute of Mechanics, Chinese Academy of Sciences, Beijing 100190, PR China

[3]School of Engineering Science, University of Chinese Academy of Sciences, Beijing 100049, PR China

(Received 11 June 2021; revised 2 January 2022; accepted 8 March 2022)

The stabilization of oblique detonation waves (ODWs) in an engine combustor is important for the successful applications of oblique detonation engines, and comprehensively understanding the effects of the inviscid reflection of ODWs on their stabilization and the relevant mechanisms is imperative to overall combustor design. In this study, the flow fields of ODW reflections in a space-confined combustor are numerically studied by solving the two-dimensional time-dependent multispecies Euler equations in combination with a detailed hydrogen combustion mechanism. The inviscid Mach reflections of ODWs before an expansion corner are emphasized with different flight Mach numbers, Ma, and different dimensionless reflection locations, $\zeta \geq 0$ ($\zeta = 0$: the ODW reflects precisely at the expansion corner; $\zeta > 0$: the ODW reflects off the wall before the expansion corner). Two kinds of destabilization phenomena of the inviscid Mach reflection of an ODW induced by different mechanisms are found, namely wave-induced destabilization at large $\zeta > 0$ for moderate (not very low) Ma and inherent destabilization at any $\zeta > 0$ for low Ma. Wave-induced destabilization is attributed to the incompatibility between the pressure ratio across the Mach stem and its relative propagation speed, which is triggered by the action of the secondary reflected shock wave or the transmitted Mach stem on the subsonic zone behind the Mach stem. Inherent destabilization is demonstrated through an in-depth theoretical analysis and is attributed to geometric choking of the flow behind the Mach stem.

Key words: detonation waves

† Email address for correspondence: cywen@polyu.edu.hk

1. Introduction

Detonation waves are supersonic combustion waves that can sustain themselves in a premixed combustible mixture (Zhang, Ng & Lee 2012; Zhang *et al.* 2014; Shi, Uy & Wen 2020). Due to their self-ignition, fast energy release and high thermal cycle efficiency, detonation phenomena as a combustion mode have attracted increasing attention in the development of hypersonic propulsion systems (Kailasanath 2000; Wolański 2013; Lu & Braun 2014). Among the different kinds of detonation-based engines (Roy *et al.* 2004; Higgins 2006; Ma *et al.* 2020), the oblique detonation engine (ODE) is expected to have more applications in hypersonic air-breathing propulsion at high flight Mach numbers because of the additional stabilization and reduced compression losses of oblique detonation waves (ODWs) (Qin & Zhang 2018; Ren *et al.* 2019; Jiang *et al.* 2021). Hence, a comprehensive understanding of ODWs is fundamental for their successful utility in ODEs, and substantial progress in understanding ODWs has been achieved in recent decades. For example, Li, Kailasanath & Oran (1994) conducted numerical simulations in which wedge-induced ODWs were found to be initiated from a non-reactive oblique shock wave (OSW), which was confirmed by subsequent experimental observations (Viguier *et al.* 1996; Lin, Zhang & Zhou 2007; Han 2013). The detailed initiation structures of ODWs were further classified into two patterns, namely smooth and abrupt OSW–ODW transition patterns (Teng & Jiang 2012; Miao *et al.* 2018; Teng *et al.* 2021). With regard to the initiation mechanisms of ODWs, their initiation can be controlled by chemical kinetics or wave dynamics depending on different free-stream parameters and mixture reactivities (Teng, Ng & Jiang 2017; Zhang *et al.* 2019). Moreover, similar to normal detonation waves (NDWs), ODW surfaces are always inherently unstable and composed of multiscale cell-like structures and moving transverse waves (Choi *et al.* 2007; Han, Wang & Law 2019; Yang *et al.* 2019*b*).

Among the various key techniques required for the development of an air-breathing detonation-based engine (Schwartzentruber, Sislian & Parent 2005; Alexander, Sislian & Parent 2006; Wolański 2013; Zhang *et al.* 2020*b*, 2022), detonation-stabilization control is imperative to the engine's stable operations; nevertheless, achieving such control remains challenging because of the fast response of detonation waves to the incoming flow conditions and the extremely high relative propagation speed (thousands of metres per second). To stabilize an NDW in an engine combustor, the key point is to match the detonation propagation speed (always overdriven) with the incoming flow speed. If the propagation speed of the NDW is greater than the flow speed in the combustor, the NDW propagates upstream; conversely, the NDW attenuates downstream if its propagation speed is lower than that of the incoming flow. To dynamically stabilize the detonation in the engine combustor, Cai *et al.* (2016, 2019, 2021) employed a cavity as a flame holder to support an NDW in the supersonic incoming flow and used an expansion wall to attenuate the detonation wave downstream; the opposing effects of the cavity and the expansion wall on the propagation of the detonation wave compete and ultimately equilibrate with each other, which facilitates the stabilization of the NDW in the combustor. Moreover, Cai *et al.* (2020) further attempted to control the propagation of an NDW in a straight channel by setting a series of suction slots behind the detonation front; their numerical results suggested that the dynamic stabilization of the detonation wave can be achieved.

Many experiments (Sterling *et al.* 1998; Verreault & Higgins 2011; Maeda, Kasahara & Matsuo 2012; Maeda *et al.* 2013) and simulations (Teng *et al.* 2017; Han *et al.* 2019; Yang, Ng & Teng 2019*a*) have previously been conducted on the stabilization of ODWs, suggesting that it is easy to stabilize an ODW over isolated wedges or cones, which is one of the major advantages of ODEs. However, the stabilization of an ODW induced

by an isolated wedge or cone is only a typical external flow problem, whereas the stabilization of an ODW in an ODE combustor is an internal flow problem because of the geometric constraints of the combustor's internal walls. In particular, the additional factors involved in internal flows, such as the reflection of OSWs/ODWs (Wang *et al.* 2020*a*,*b*; Wang, Yang & Teng 2021), shock/detonation–shock/detonation interactions (Xiang *et al.* 2021*a*,*b*), shock/detonation–boundary layer interactions (Cai *et al.* 2017, 2018*a*,*b*) and shock/detonation-induced boundary layer separation (Ess, Sislian & Allen 2005; Miao *et al.* 2020), increase the flow complexity in a space-confined combustor and cannot be overlooked in the stabilization of ODWs. These fundamental differences in detonation stabilization between spatially confined and unconfined flow regimes were also pointed out by Higgins (1997) through experiments, where hypervelocity blunt projectiles were fired into detonation chambers with significantly different chamber diameters and various detonation propagation phenomena were observed. In early experimental investigations of ram accelerators (e.g. Knowlen *et al.* 1995; Higgins, Knowlen & Bruckner 1998; Yatsufusa & Taki 2002), which share geometries similar to those of ODE combustors, it was demonstrated that boundary layer separation induced by shock waves and/or combustion is always responsible for the upstream motion of shock waves over the projectiles, resulting in the unstart phenomena and, consequently, the failure of acceleration and operation. Moreover, the effects of multiple shock reflections on the upstream propagation of ODWs over projectiles in superdetonative ram accelerators and even unstart of the systems have also been noted in experiments (Seiler *et al.* 1998, 2000). Therefore, despite the inherent stability of ODWs in an unconfined space, their stabilization control is always necessary in an ODE combustor; to this end, it is valuable to comprehensively understand the effects of the aforementioned factors on the stabilization of ODWs and the relevant mechanisms.

The effects of boundary layer separation on the failures of ramjets and scramjets have also been well documented in the literature (Curran & Murthy 2001; Im & Do 2018; Seleznev, Surzhikov & Shang 2019). Accordingly, various techniques, such as boundary layer blowing/bleeding and mass flow spillage, have been proposed and successfully applied (Chang *et al.* 2017; Urzay 2018). Recently, these techniques have also been employed to overcome separation-induced destabilization of ODWs in ODE combustors. For example, Alexander & Sislian (2008) and Wang & Sislian (2010) employed an air jet to blow down the boundary layer upstream of the ODW reflection locus to suppress the detonation-induced separation of the boundary layer. Zhang *et al.* (2020*b*, 2021*b*, 2022) adopted a floor bleed structure at the combustor's entrance to spill out the incoming boundary layer from the inlet; as a consequence, the continuous upstream motion of the boundary layer separation bubble, also induced by the reflection of the ODW, ceases at the entrance because of the interruption of the boundary layer. With boundary layer separation being addressed properly, destabilization of the flow field in the ODE combustor may still occur under the influences of the aforementioned inviscid factors (i.e. shock/detonation reflections, shock/detonation–shock/detonation interactions). In other words, the inviscid stabilization of ODWs, which is related to the geometric structure of the combustor, appears as a precondition of overall stabilization and must be considered prior to adopting other stabilization-control measures in the design of an ODE combustor.

Wave reflection is a major feature in the inviscid ODW flow field in a space-confined ODE combustor (Lu, Fan & Wilson 2006; Wang *et al.* 2021; Xiang *et al.* 2021*b*), and its effects on ODW stabilization and the relevant mechanisms are important for the initial geometric design of the engine combustor. Figure 1 schematically shows two typical configurations of ODEs presented in previous literature (Schwartzentruber *et al.* 2005; Alexander *et al.* 2006; Wolański 2013), namely the external-compression ODE and the

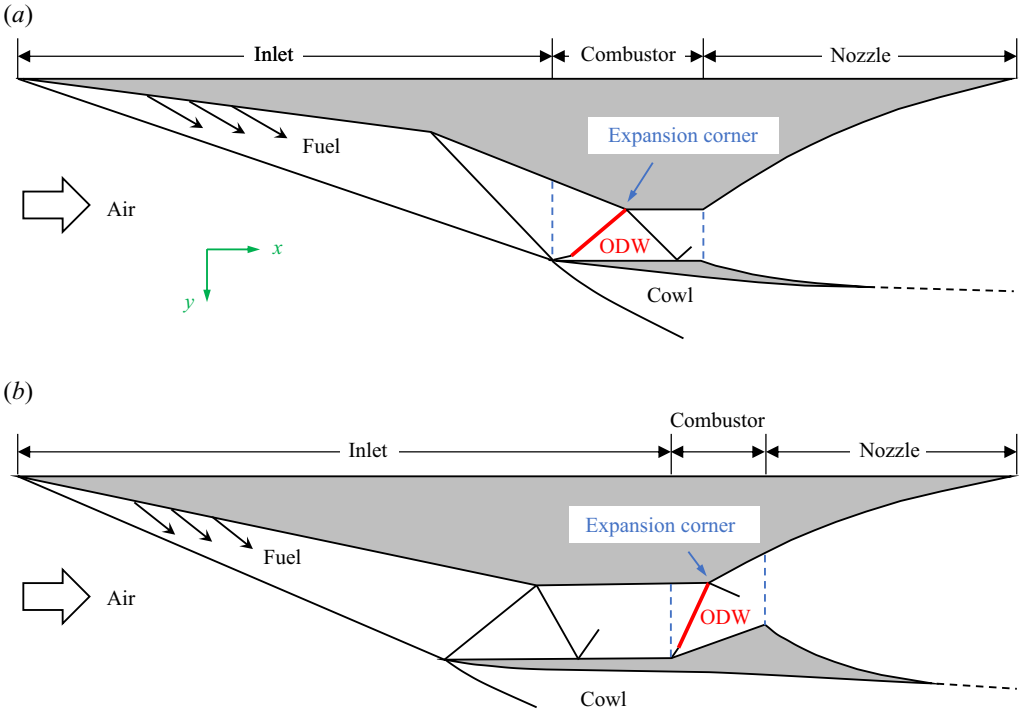

Figure 1. Schematics of two typical configurations of ODEs. (*a*) external-compression ODE. (*b*) Mixed-compression ODE.

mixed-compression ODE. These two types of ODEs have an obviously similar flow pattern of ODW reflection in the combustor; that is, the ODW reflects over an internal wall with an expansion corner, and the ideal reflection locus is precisely at the expansion corner. However, due to the general unsteadiness of the high-speed fuel–air mixture flowing into the combustor and/or the potential off-design operation of the engine (Yang *et al.* 2019*a*, 2021; Ren, Wang & Zheng 2021), it is impossible to ensure that the ODW always reflects exactly at the expansion corner, implying that the ODW always reflects before or behind the expansion corner. Therefore, it is imperative to investigate the effects of the position of the reflection point relative to the expansion corner and other geometric parameters on the ODW flow structure in the combustor and to analyse the relevant stabilization characteristics. Because of the release of heat, a Mach reflection pattern can appear easily when the ODW reflects off a wall, and a Mach stem (MS; which is, in fact, an overdriven NDW) forms as a result. Due to the existence of a subsonic zone behind the MS, downstream disturbances may propagate upstream to the detonation front and consequently destabilize the ODW reflection pattern, eventually causing the ODE to fail. Accordingly, this paper mainly investigates the relevant flow structures, stabilization characteristics and inherent mechanisms of a Mach reflection occurring more easily when the ODW reflects off the wall before the expansion corner.

The remainder of this paper is organized as follows. The numerical details, including the geometry of the simulated ODE combustor, the numerical methods and the cases considered herein, are briefly introduced in § 2. Next, the flow fields and the relevant stabilization characteristics of ODWs that reflect precisely at the expansion corner at different flight Mach numbers are discussed in § 3.1. Then, the flow structures of the

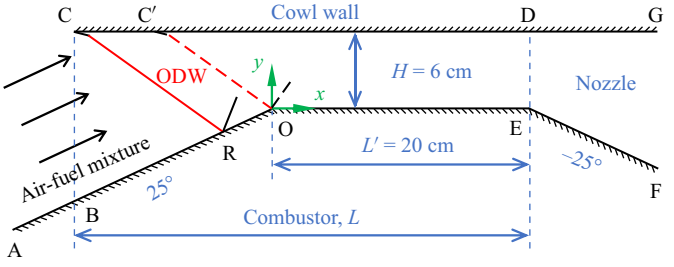

Figure 2. Detailed geometry of the combustor of an external-compression ODE.

stabilized Mach reflection of an ODW reflecting before but close to the expansion corner and the evolutions of the relevant MS are presented in § 3.2. Thereafter, the evolutions of the destabilized Mach reflection of an ODW reflecting far upstream of the expansion corner and the relevant destabilization mechanism are analysed in § 3.3. In § 3.4, the inherent destabilization phenomenon of the Mach reflection of an ODW at a low flight Mach number is investigated, followed by a discussion of its relevant mechanism in § 3.5 with a formulation providing the stabilized locations of the MS. Finally, the conclusions are presented in § 4.

2. Physical and mathematical models

Since the flow patterns of ODW reflection are similar in the combustors of both configurations of ODEs (figure 1), the combustor of an external-compression ODE, whose detailed geometry is shown in figure 2, is taken as an example in this study. As shown in figure 2, the combustor is contained within points $\overline{\mathrm{DCBOE}}$, where point C is the leading tip of the cowl and point O is the expansion corner with an expansion angle of 25°. $\overline{\mathrm{CD}}$ or $\overline{\mathrm{CG}}$ represents the engine's cowl wall. $\overline{\mathrm{BO}}$ is one part of the combustor's lower wall before the expansion corner with an inclination angle of 25°, while $\overline{\mathrm{OE}}$ (which is parallel to the cowl wall) is the other part behind the expansion corner. $\overline{\mathrm{EF}}$ is a part of the nozzle's wall with an expansion angle of 25°, while $\overline{\mathrm{AB}}$ is a part of the inlet's wall sharing the same inclination angle as $\overline{\mathrm{BO}}$. The height ($\overline{\mathrm{DE}}$) of the combustor's straight channel is $H = 6$ cm, while its length ($\overline{\mathrm{OE}}$) is $L^{'} = 20$ cm. The total length of the combustor L depends on the designed reflection locus of the ODW (i.e. point R), which varies among the different cases considered in this study. A similar ODE combustor geometry has been adopted for previous studies by the authors (Zhang *et al.* 2020*b*, 2021*b*).

The effects of ODW reflection on the stabilization/destabilization characteristics of ODWs as well as the inviscid destabilization mechanisms are emphasized in this study; hence, viscous effects are neglected. However, the effects of viscosity on the transition between regular and Mach reflections should be noted. It has been demonstrated that shock-induced boundary layer separation has significant effects on the shifting of the dual-solution regime of inert shock-wave reflections (Tao, Fan & Zhao 2014; Matheis & Hickel 2015; Grossman & Bruce 2018; Xue, Wang & Cheng 2021). That is, it delays the transition from regular to Mach reflection, and its effect on the transition from Mach to regular reflection is inverse (i.e. promotion). For ODW reflection transitions, although similar viscous effects may be expected, the specific transition criteria are not the main focus of this study. Therefore, the complex effects of boundary layer separation on ODW reflection transitions are not considered but, instead, will be further studied in the future. Without considering viscous effects, two-dimensional time-dependent

multispecies reactive Euler equations (Fang *et al.* 2019; Teng, Liu & Zhang 2020) are solved. Jachimowski's H_2 combustion mechanism (Wilson & Maccormack 1992), which involves 19 reversible elementary reactions among 9 species (H_2, H, O_2, O, OH, HO_2, H_2O_2, H_2O and N_2), is adopted to model the combustion rates. This detailed chemical reaction mechanism has been demonstrated to be capable of providing experimentally consistent laminar flame speeds, adiabatic flame temperatures and ignition delay times (Jachimowski 1988) and has been widely applied in simulations of scramjets (Fureby *et al.* 2011; Chapuis *et al.* 2013), shock-induced combustion (Choi, Jeung & Yoon 2000; Teng *et al.* 2020) and detonation (Choi, Shin & Jeung 2009; Zhang *et al.* 2020*b*, 2021*b*).

It should be noted that the temperature behind the detonation wave of a H_2–air mixture can reach 3000 K or higher; hence, vibration excitations of some involved polyatomic species (i.e. O_2, N_2, H_2O, HO_2 and H_2O_2) with relatively low vibrational characteristic temperatures become noticeable. To include the excited vibrational energies and other energy modes in the internal energy of each species, in this study, the species thermodynamic database of NASA (McBride, Gordon & Reno 1993) is employed to evaluate the equilibrium thermodynamic properties of each species by a piecewise fourth-order polynomial of temperature. In recent studies (Shi *et al.* 2017, 2020; Uy *et al.* 2020), thermal non-equilibrium has been demonstrated to have non-negligible effects on detonation instabilities and the resulting detonation cellular structures in a multidimensional space. However, the aforementioned detonation dynamic features are not the main focus of this study. Moreover, a comparison of the flow fields in a similar ODE combustor under thermal equilibrium and non-equilibrium conditions (conducted in the authors' previous study: Zhang *et al.* (2021*b*)) showed that the overall flow structures or their stabilization characteristics are not significantly affected by thermal non-equilibrium effects. Therefore, thermal non-equilibrium effects are neglected in the present modelling; that is, all simulation results discussed in this study are under the thermal equilibrium assumption.

A quadrilateral grid-based finite-volume method (Chakravarthy 1999) is employed to numerically solve the governing equations. A second-order upwind total variation diminishing scheme is used to spatially discretize the equations, and the nonlinear Harten–Lax–van Leer contact approximate Riemann solver (Toro 2013) is adopted to evaluate the interface fluxes to satisfy the entropy and positivity conditions simultaneously. Additionally, to suppress spurious oscillations near flow discontinuities, a minmod-type limiter is used. In the time direction, the equations are explicitly integrated by the fourth-order Runge–Kutta method, and an operator-splitting method (Ropp & Shadid 2009) is employed to treat the chemical source terms, which always cause stiffness problems originating from the mismatch of the time scales between chemical reactions and flows.

In the present study, numerical simulations are carried out with different flight Mach numbers and different designed ODW reflection locations before or precisely at the expansion corner, as summarized in table 1. Notably, in classic shock reflection configurations in which an OSW generated by a finite wedge impinges on a flat surface, the height of the MS depends on the height of the flow path (i.e. the vertical distance from the wedge tail to the flat surface) (Li & Ben-Dor 1997; Ben-Dor 2007; Mouton & Hornung 2007). According to shock reflection theory (Ben-Dor 2007), the formation of a sonic throat under the interaction between the expansion fan and the slip line (SL) is important to the stabilized location and, consequently, the stabilized height of the MS. In such a type of shock reflection configuration, the expansion fan emits from the tail of the finite wedge on the opposite side of the reflection locus; hence, the interaction between

the expansion fan and the SL depends on the vertical distance from the wedge tail to the flat surface. As a result, the height of the MS in such configurations depends on the height of the flow path. Comparatively, in the ODW reflection configuration depicted in figure 2, the expansion fan emits from an expansion corner on the same side of the reflection locus. As a result, the stabilized height of the MS discussed in this study (if not influenced by downstream wave structures) does not depend on the height of the combustor's straight channel (i.e. H) but on the designed reflection location of the ODW (i.e. $\overline{\mathrm{RO}}$). However, destabilization of ODW Mach reflection may still be caused by downstream wave structures that result from the multiple reflections of shock waves between the combustor's walls. Obviously, with the designed reflection location of ODW unchanged, the relative locations of these downstream wave structures to the expansion corner are determined by the channel's height. In other words, the stabilization/destabilization characteristics of ODWs in the combustor considered in this study depend on not only the designed reflection location but also the geometric scale of the combustor (i.e. the height of the combustor's straight channel, H). Hence, to present and discuss the results in a more general way, the non-dimensional parameter ζ is introduced in this study to describe the relative location of the designed ODW reflection point:

$$\zeta = \frac{\overline{\mathrm{RO}}}{H}. \tag{2.1}$$

A value of $\zeta = 0$ means that the ODW reflects exactly at the expansion corner (the dashed red line in figure 2), while $\zeta > 0$ implies that the ODW reflects off the wall before the expansion corner, as shown by the solid red line in figure 2. Notably, without considering the chemical reaction characteristic length scales (i.e. in cold or chemical equilibrium flows), the non-dimensionalization of (2.1) is justifiable. The flow field in the combustor should depend on the non-dimensional parameter ζ, rather than the dimensional reflection location or channel height individually. In the present study, because chemical non-equilibrium effects are not dominant (i.e. near-equilibrium overall, to be discussed later in § 3.1), (2.1) still approximately holds, and the overall flow fields with the same ζ value but different channel heights should be similar.

Notably, the exact reflection locations of ODWs on the wall (i.e. $\overline{\mathrm{RO}}$) and the subsequent ζ values are difficult to determine when Mach reflection occurs or the flow structures in the combustor become destabilized because an MS forms before the ODW reflecting off the wall, or the ODW is even non-stationary. To overcome this difficulty, a preinvestigation simulation of a pure ODW induced only by the cowl wall (i.e. $\overline{\mathrm{CD}}$) is conducted for each flight Mach number without considering the combustor's lower wall (i.e. $\overline{\mathrm{BOE}}$), and the corresponding reflection locus of the ODW (i.e. point R) is determined by its intersection point with the location at which $\overline{\mathrm{BOE}}$ should be. Note again that the ζ values discussed in this study are generally smaller than one; hence, ζ values of different cases are expressed in fractional terms with a constant denominator of 60 (i.e. the channel height of 60 mm) in table 1 and the remainder of this paper, for intuitional comparison.

Four flight Mach numbers, namely 9, 9.5, 10 and 10.5, are taken into account, and the flight altitude is fixed at 30 km for the ODE. Since this study focuses on the effects of reflection on the stabilization characteristics of ODWs in a space-confined ODE combustor and the relevant inherent mechanisms of stabilization/destabilization, the complex processes of fuel (H_2) injection and its subsequent mixing with air in the ODE inlet are not considered here. Rather, following the simplification of the inflow of the ODE combustor in previous studies (Ren *et al.* 2018; Fang *et al.* 2019; Xiang *et al.* 2019), the free stream of the high-altitude atmosphere is assumed to be precompressed twice by two weak

Case no.	Ma	T_{in} (K)	p_{in} (kPa)	V_{in} (m s^{-1})	$\overline{\mathrm{RO}}$ (mm)	ζ value
1	9	855.1	43.96	2466	0	0
2	9	855.1	43.96	2466	1	1/60
3	9	855.1	43.96	2466	3	3/60
4	9	855.1	43.96	2466	6	6/60
5	9	855.1	43.96	2466	12	12/60
6	9.5	909.2	49.52	2608	0	0
7	9.5	909.2	49.52	2608	1	1/60
8	9.5	909.2	49.52	2608	3	3/60
9	9.5	909.2	49.52	2608	5	5/60
10	9.5	909.2	49.52	2608	8	8/60
11	9.5	909.2	49.52	2608	15	15/60
12	10	965.2	55.47	2751	0	0
13	10	965.2	55.47	2751	2	2/60
14	10	965.2	55.47	2751	5	5/60
15	10	965.2	55.47	2751	10	10/60
16	10	965.2	55.47	2751	20	20/60
17	10	965.2	55.47	2751	30	30/60
18	10.5	1023.1	61.83	2893	0	0
19	10.5	1023.1	61.83	2893	5	5/60
20	10.5	1023.1	61.83	2893	10	10/60
21	10.5	1023.1	61.83	2893	20	20/60
22	10.5	1023.1	61.83	2893	30	30/60

Table 1. Summary of the flight Mach numbers, the inflow parameters of the combustor and the designed ODW reflection locations for different cases.

OSWs generated by the two 12.5° ramps in the inlet (see figure 1*a*), and the injection of H_2 and its subsequent mixing with air are assumed to be completed downstream of these two OSWs and before entering the ODE combustor. Consequently, a uniformly premixed stoichiometric H_2–air inflow is assumed to enter the combustor parallel to the end of the inlet and the wall before the expansion corner (i.e. 25° with respect to the x direction), and this serves as the inflow condition for the simulations in this study, as shown in figure 2. The corresponding inflow parameters for the different flight Mach numbers are summarized in table 1. Note again that the vibrational relaxation time scales of H_2–air mixture in the inlet are significantly smaller than the corresponding flow residence time scale; hence, it is reasonable to set the inflow of the combustor (i.e. the outflow of the inlet) to be under thermal equilibrium.

For the other boundary conditions, the slip wall condition is set at all wall boundaries due to the assumed inviscid flow, and the supersonic outflow condition is set at all outflow boundaries. Quadrilateral grid cells are used in this study, and the characteristic grid size in the main combustion zone is set as 0.1 mm, which has been carefully validated by resolution tests to exclude the grid dependence of the simulation results. One of these grid resolution studies is presented in § 3.2 as an example.

3. Results and discussion

3.1. *Stabilized reflection of ODWs with $\zeta = 0$*

The reflection patterns of ODWs in the combustor at different flight Mach numbers with the reflection point located precisely at the expansion corner (i.e. $\zeta = 0$) are analysed first. The time-dependent simulation results suggest that the flow structures with $\zeta = 0$ all

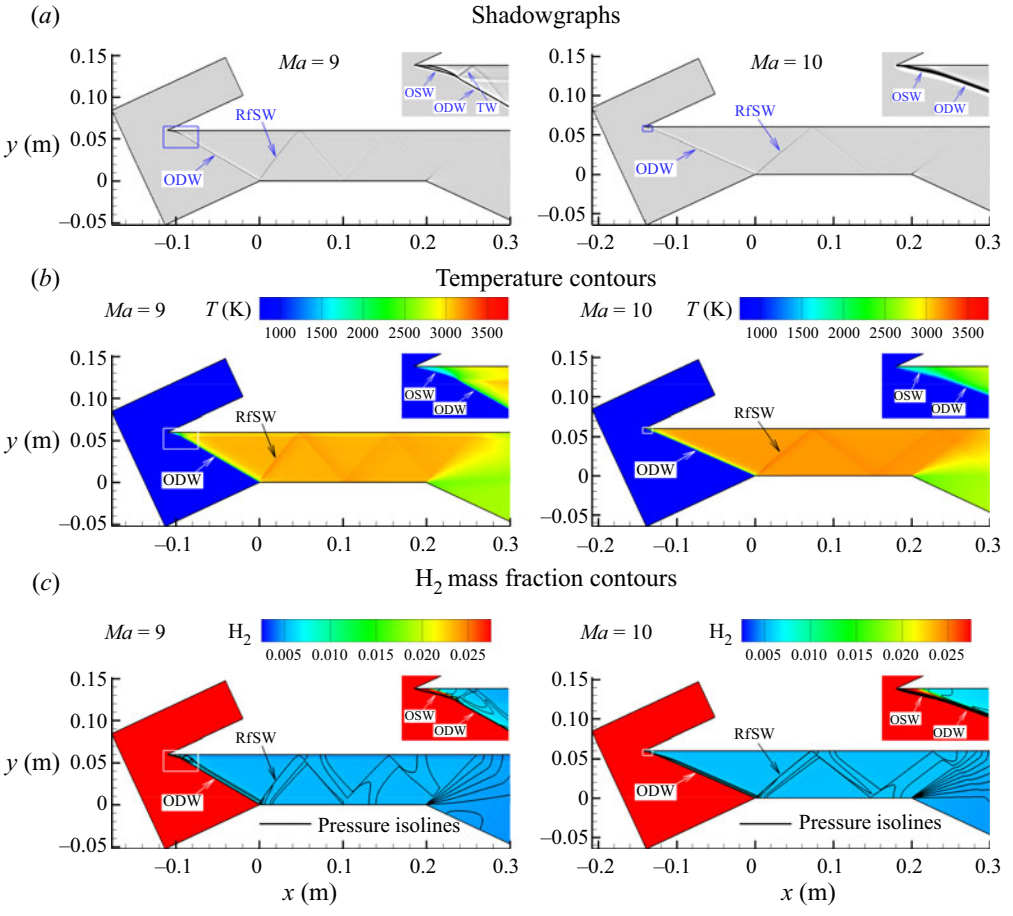

Figure 3. Flow fields of the stabilized reflection of ODWs with $\zeta = 0$ at $Ma = 9$ (left) and $Ma = 10$ (right): (*a*) shadowgraphs, (*b*) temperature contours and (*c*) H_2 mass fraction contours.

remain stabilized in the combustor at the investigated Mach numbers (9, 9.5, 10 and 10.5). Taking $Ma = 9$ and 10 as examples, the stabilized flow structures are depicted in figure 3 by shadowgraphs, temperature contours, H_2 mass fraction contours and pressure isolines. When the high-speed premixed H_2–air mixture flows into the combustor, an OSW first forms over the leading tip of the cowl, inducing combustion of the mixture downstream. Away from the cowl wall, the combustion zone approaches the OSW front and eventually interacts with the shock-wave front over a short distance. Consequently, the flame front is coupled tightly with the OSW front, and the shock-wave angle increases, implying the formation of an ODW. Across this ODW, the flow temperature abruptly increases to approximately 3000 K, and the H_2 mass fraction drops to a rather low level; these phenomena are the other two typical features of a detonation wave. Then, the ODW reflects at the expansion corner within the combustor, forming a reflected shock wave (RfSW), which is weak due to the parallel geometry of the flow channel behind the expansion corner. Downstream in the combustor, the RfSW reflects repeatedly between the internal walls and further weakens gradually before it meets another expansion fan at the outlet of the combustor. Finally, the high-temperature combustion products exit the combustor and expand and accelerate in the nozzle.

A comparison of the flow structures between these two Mach numbers in figure 3 reveals that the initiation length under $Ma = 10$ is shorter than that under $Ma = 9$. A transverse wave (TW) connecting to the OSW–ODW transition point exists in the case of $Ma = 9$, implying an abrupt OSW–ODW transition pattern at this relatively low Mach number, while no obvious TW can be observed within the initiation zone in the case of $Ma = 10$, meaning the OSW–ODW transition pattern at this relatively high Mach number is smooth. These findings regarding the ODW initiation structure coincide with those found in previous numerical studies (Teng & Jiang 2012; Teng *et al.* 2017, 2021). Notably, as compared to the geometric scales of the combustor, the OSW–ODW transition zones are rather small, implying that the overall flow fields in the combustor are in near-equilibrium states, although some non-equilibrium effects still occur locally. Further, a higher Mach number leads to a smaller oblique detonation angle, and thus the leading tip of the cowl occurs farther upstream from the expansion corner for $\zeta = 0$ (with the same height of the combustor). Additionally, the RfSW angles and its further reflected shocks are smaller for higher Mach numbers. Moreover, the combustion temperature in the combustor at $Ma = 10$ is slightly higher than that at $Ma = 9$, which is attributed to the higher total temperature but the same deflection angle of the inflow entering the combustor.

3.2. *Stabilized Mach reflection of ODWs with small $\zeta > 0$*

When the ideal reflection point of the ODW is located on the wall before the expansion corner (i.e. for $\zeta > 0$), the Mach reflection pattern of the ODW coincides with the formation of an MS. For small $\zeta > 0$, the flow field under $Ma = 10$ and $\zeta = 10/60$ is taken as an example. Figure 4 depicts the evolution of the flow field in this case by shadowgraphs overlaid with sonic lines. To quantitatively exhibit the evolution of the formed MS and the stabilization characteristics of the Mach reflection of the ODW, the temporal evolutions of the location and corresponding motion speed of the pressure-jump point along the wall before the expansion corner are plotted in figure 5, where the location of the pressure-jump point is evaluated according to its distance from the expansion corner. Obviously, this pressure-jump point represents the location of the ODW reflection point for a regular reflection pattern or the location of the MS for a Mach reflection pattern. Therefore, figure 5 also presents the temporal evolutions of the formed MS when a Mach reflection pattern appears in the late period of the evolution of the flow field. In addition, points at different time instants corresponding to the shadowgraphs shown in figure 4 are also marked on the motion speed curve in figure 5 for convenience.

As indicated in figure 4(*a*), after the ODW has formed over the cowl's internal wall but before it becomes fully established, its reflection point is located on the wall behind the expansion corner, and no pressure jump occurs along the wall before the expansion corner. At this moment, the location of the pressure-jump point and its corresponding motion speed are simply set to zero (point 'a' in figure 5). Hence, when the ODW reflects precisely at the expansion corner later in its evolution (figure 4*b*), the motion speed of the pressure-jump point abruptly rises (point 'b' in figure 5). Next, a regular reflection pattern occurs over the wall before the expansion corner (figure 4*c*) because of the relatively small oblique detonation angle of the tail of the ODW during its evolution, and the reflection point moves upstream along the wall continuously with a gradually decreasing motion speed (point 'c' in figure 5). Then, the regular reflection pattern of the ODW transits to a Mach reflection pattern (figure 4*d*), and the motion speed of the pressure-jump point reaches another obvious peak (point 'd' in figure 5) during the transition process. As depicted in figures 4(*e*) and 4(*f*), an MS forms and grows thereafter while continuously moving upstream along the wall, which is again accompanied by a decreasing

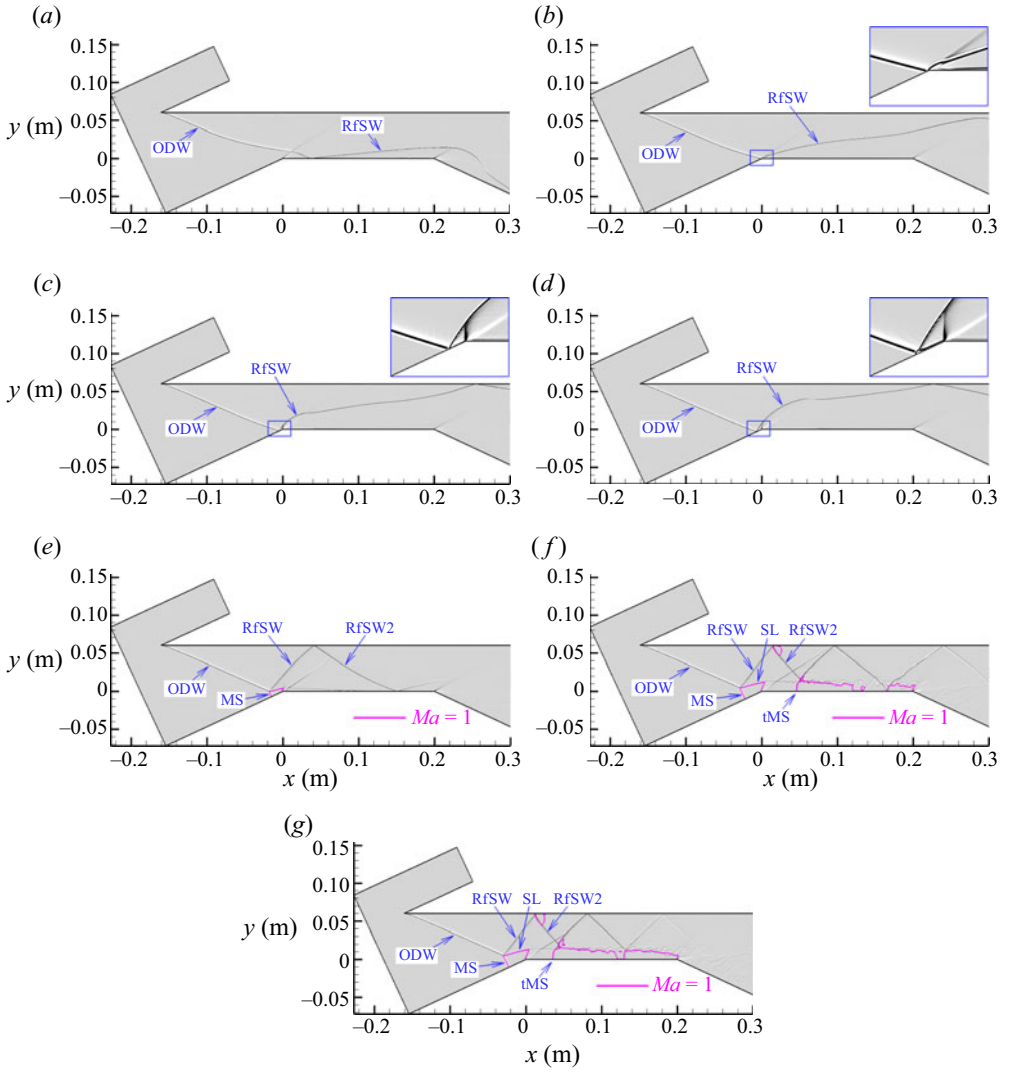

Figure 4. Evolution of the flow field (shadowgraphs) of the stabilized Mach reflection of an ODW at $Ma = 10$ and $\zeta = 10/60$: (*a*) $t = 0.068$ ms, (*b*) $t = 0.101$ ms, (*c*) $t = 0.116$ ms, (*d*) $t = 0.131$ ms, (*e*) $t = 0.208$ ms, (*f*) $t = 0.760$ ms and (*g*) $t = 1.581$ ms.

motion speed. In addition to the formation of the MS and RfSW connected to the triple point, an SL is also emitted from the triple point in the Mach reflection pattern of the ODW, thereby separating the flows across the ODW and MS. When the RfSW of the ODW reflects off the cowl wall, a secondary reflected shock wave (RfSW2) forms and reflects later over the SL, forming another reflected shock wave and, notably, a transmitted MS (tMS) between the SL and the lower wall of the combustor. As indicated in figure 5, after the formation of the Mach reflection pattern, the motion speed of the formed MS rapidly drops and then gradually decreases towards zero. After a sufficiently long period, the motion speed of the MS finally drops to zero, with the MS finally reaching its most upstream location. As a result, all the flow structures remain stabilized in the combustor, and the flow field reaches its steady state, as shown in figure 4(*g*).

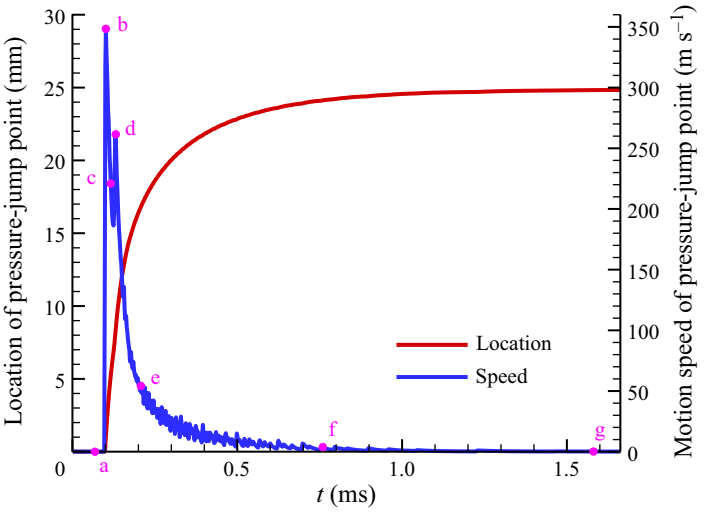

Figure 5. Evolutions of the location and corresponding motion speed of the pressure-jump point along the wall before the expansion corner of the stabilized Mach reflection of ODWs at $Ma = 10$ and $\zeta = 10/60$.

The temperature and H_2 mass fraction contours along with the pressure isolines of the final steady flow field in this case are exhibited in figure 6. As indicated in figures 4(*g*) and 6, in addition to the ODW, a high temperature reaching approximately 3500 K and a rather low H_2 mass fraction are also featured just behind the MS, implying the tight coupling between the flame front and the MS. In other words, the MS is an overdriven NDW. According to Zhang *et al.* (2021*b*), two stabilized detonation combustion modes, namely the oblique detonation combustion mode and the normal detonation combustion mode, simultaneously exist in the ODE combustor in this case. Moreover, a subsonic zone capable of propagating pressure waves upstream exists behind the MS and extends to the expansion fan emitting from the expansion corner (figure 4*g*). However, no obvious downstream pressure wave acting on or propagating in the subsonic zone is observed, and hence the MS is not disturbed and remains stabilized at a certain position before the expansion corner.

To exclude the dependence of the simulation results on the grid size, grid resolution tests are carefully carried out by halving the sizes of the quadrilateral grid cells in both directions, leading to characteristic grid sizes of 0.05 mm in the main combustion zone for the fine grids and 0.1 mm for the coarse grids. As a result, the total number of fine grid cells is almost four times that of coarse grid cells. Taking the case of $Ma = 10$ and $\zeta = 10/60$ as an example again, comparisons of the flow fields obtained with different grid sizes are shown in figure 6, while comparisons of the flow parameter distributions are depicted in figure 7. Differences in the flow structures are difficult to distinguish by using different grid sizes. Furthermore, the distribution curves of the various flow parameters obtained with different grid sizes almost overlap with each other, especially the locations of the jumps or drops of the flow parameters, implying that the simulations accurately capture the locations of key flow structures such as detonation fronts and shock waves. Therefore, a coarse grid with a characteristic grid size of 0.1 mm is sufficient to resolve the key flow features and is adopted in this study.

It should be noted that, although the overall flow structures concerned in this paper are shown to be independent of grid size approximately when a characteristic grid size of 0.1 mm is used, this grid size is still not fine enough to precisely predict the

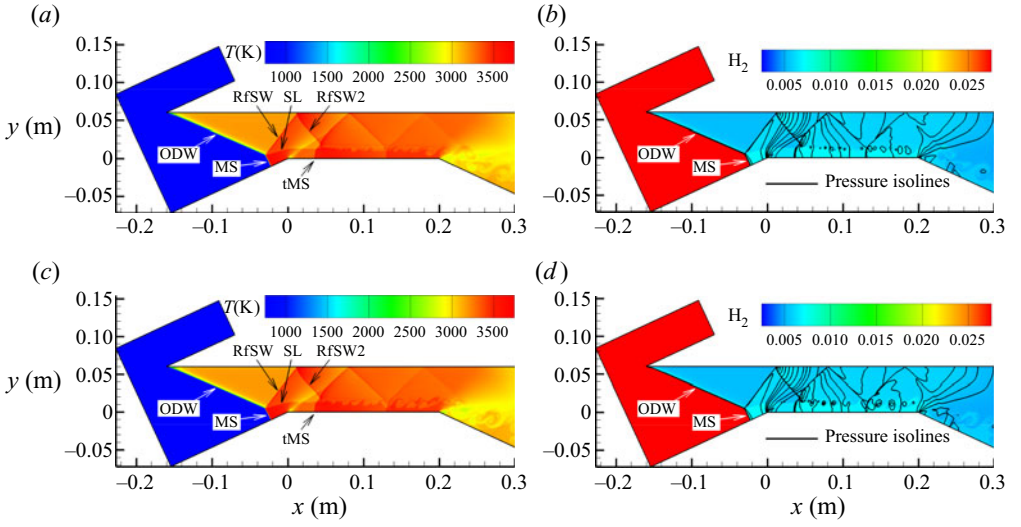

Figure 6. Contours of the temperature and H_2 mass fraction of the stabilized Mach reflection of an ODW ($Ma = 10$, $\zeta = 10/60$) at $t = 1.581$ ms with different mesh sizes: (*a*) temperature contour ($\Delta x = 0.1$ mm), (*b*) H_2 mass fraction contour ($\Delta x = 0.1$ mm), (*c*) temperature contour ($\Delta x = 0.05$ mm) and (*d*) H_2 mass fraction contour ($\Delta x = 0.05$ mm).

induction length of an ODW or capture the potential cellular structures on the detonation surface. The grid-size requirement for predicting the aforementioned detonation features generally needs to ensure that there are at least 20 grid points within the half reaction zone of the corresponding Chapman–Jouguet detonation wave (Teng, Jiang & Ng 2014; Shen & Parsani 2017; Shi *et al.* 2020). For example, for the inflow conditions of $Ma = 10$ listed in table 1, the length of the half reaction zone is approximately 0.4 mm, implying a minimum grid-size requirement of 0.02 mm, which is significantly smaller than that used in the present study (0.1 mm). Fortunately, the precise prediction of the induction length of an ODW does not affect the overall flow structures in the combustor, and the cellular characteristics of the detonation surfaces are not the main focus of this study; hence, a much finer grid is not employed to save computational resources.

For the other cases with small positive ζ values (i.e. $\zeta = 2/60$ and 5/60) at $Ma = 10$, the flow fields of the Mach reflection of the ODW are also stabilized, and similar flow structures can be observed, as shown in figure 8. In other words, an MS, an SL, an RfSW and a subsonic zone form near the reflection point of the ODW. Downstream of the ODW, the RfSW reflects off the cowl wall to form an RfSW2, and the RfSW2 further reflects over the SL, forming another reflected shock wave and a tMS between the SL and the lower wall of the combustor. As ζ increases, i.e. as the designed reflection point of the ODW moves upstream, the final stabilized location of the MS also moves upstream; additionally, the length of the MS increases, as does the size of the subsonic zone behind the MS. Further, the locations of the RfSW2 and tMS downstream of the subsonic zone move farther upstream and approach the subsonic zone with increasing ζ. For $Ma = 9.5$ or 10.5, the Mach reflection patterns of the ODW similarly become stabilized at small positive ζ values, as summarized in figure 9, and stabilized flow structures similar to those discussed in this section can be obtained.

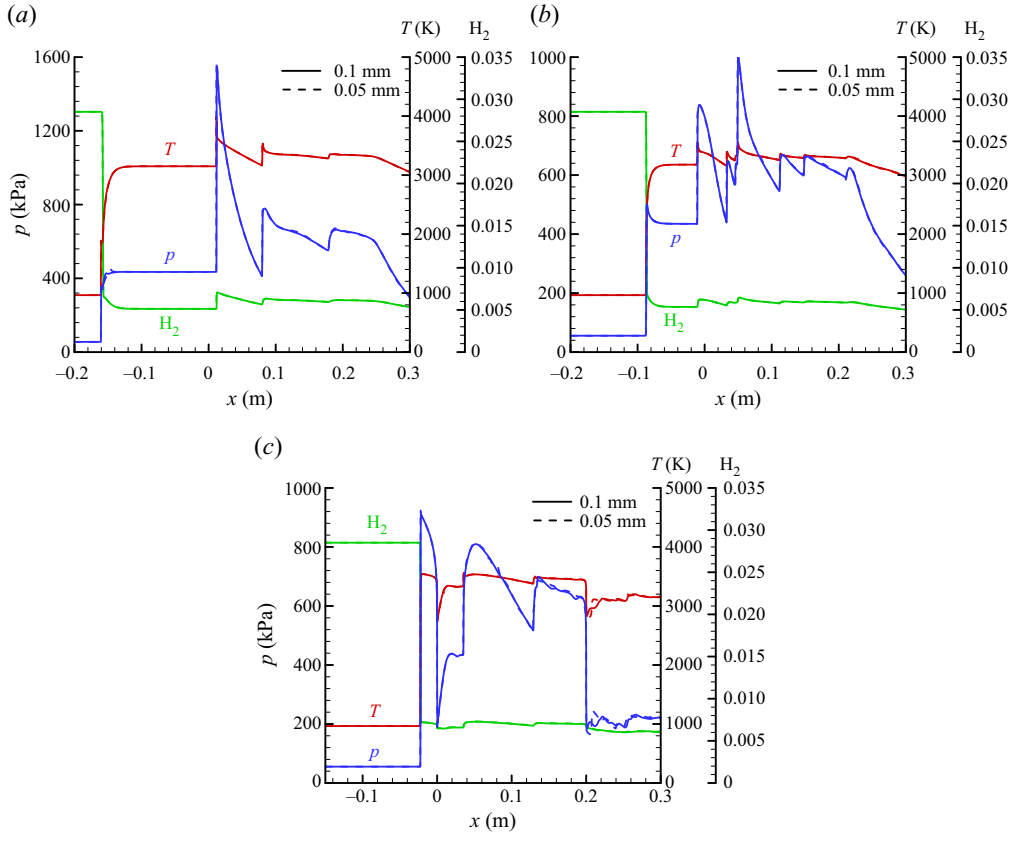

Figure 7. Flow parameter distributions for the stabilized Mach reflection of an ODW in the combustor ($Ma = 10$, $\zeta = 10/60$) at $t = 1.581$ ms with different mesh sizes: (*a*) along the cowl wall ($y = 0.06$ m), (*b*) along the central line ($y = 0.03$ m) and (*c*) along the lower walls (i.e. $\overline{AO}$, $\overline{OE}$ and $\overline{EF}$ in figure 2).

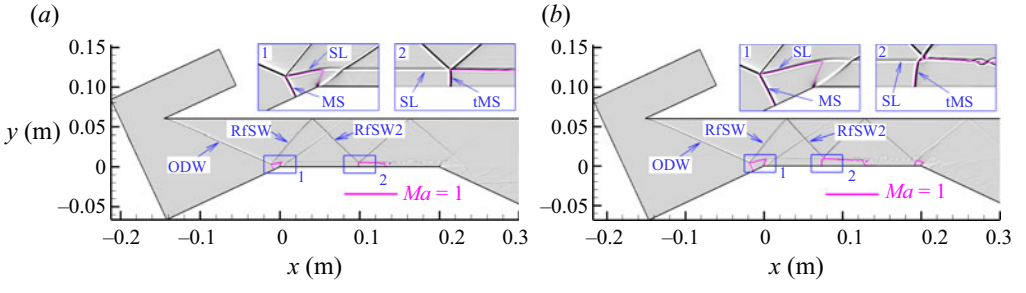

Figure 8. Shadowgraphs of the stabilized Mach reflection patterns of ODWs at $Ma = 10$: (*a*) $\zeta = 2/60$ and (*b*) $\zeta = 5/60$.

3.3. *Destabilized Mach reflection of ODWs with large $\zeta > 0$*

Again, $Ma = 10$ is taken as an example for discussion in this section. Different from the stable cases with small ζ, when ζ further increases to a larger value, for example $\zeta = 20/60$ or $30/60$, the flow field of the Mach reflection of the ODW becomes destabilized in the ODE combustor, as depicted in figure 9. Similar to figure 5, the temporal evolutions of the location of the pressure-jump point along the wall before the expansion corner and its

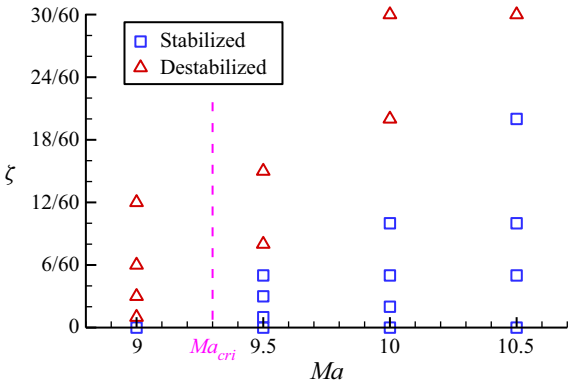

Figure 9. Summary of the stabilization characteristics of the Mach reflection of ODWs at different Ma and with different ζ values. The dashed line corresponds to the critical Mach number (i.e. $Ma_{cri} = 9.3$) predicted by the theory constructed in § 3.5.

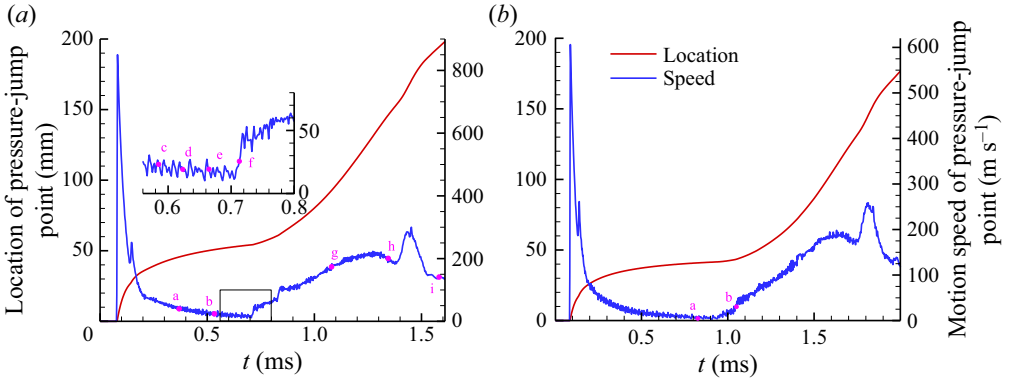

Figure 10. Evolutions of the location and corresponding motion speed of the pressure-jump point along the wall before the expansion corner of the destabilized Mach reflection of ODWs at $Ma = 10$: (*a*) $\zeta = 30/60$ and (*b*) $\zeta = 20/60$.

corresponding motion speed in the cases of $\zeta = 20/60$ and 30/60 at $Ma = 10$ are shown in figure 10. According to the above discussion in § 3.2, these curves represent the evolutions of the formed MS, where the MS forms at the time instant of the second peak in the motion speed curve. In the early period, the motion speed of the MS, which continuously moves upstream, is greater than zero but decreases, rapidly at first and then gradually. Accordingly, the upstream motion of the MS approaches zero and seemingly stops at a certain position, and the MS appears to be stabilized. However, as the flow field continues to evolve, at a certain time instant (approximately $t = 0.9$ ms for $\zeta = 20/60$ or $t = 0.7$ ms for $\zeta = 30/60$), the motion speed of the MS suddenly begins to increase, after which the MS accelerates while moving upstream. Finally, the MS moves upstream far from the expansion corner, indicating that the MS has moved out of the combustor, and the MS continues moving upstream with a very large speed. In other words, the Mach reflection of the ODW becomes destabilized in the combustor at a large value of ζ, which may lead to the engine becoming unstart. Therefore, to help design the geometry of the combustor, it is imperative to determine the mechanisms responsible for the destabilized Mach reflection of ODWs as well as the relevant influencing factors.

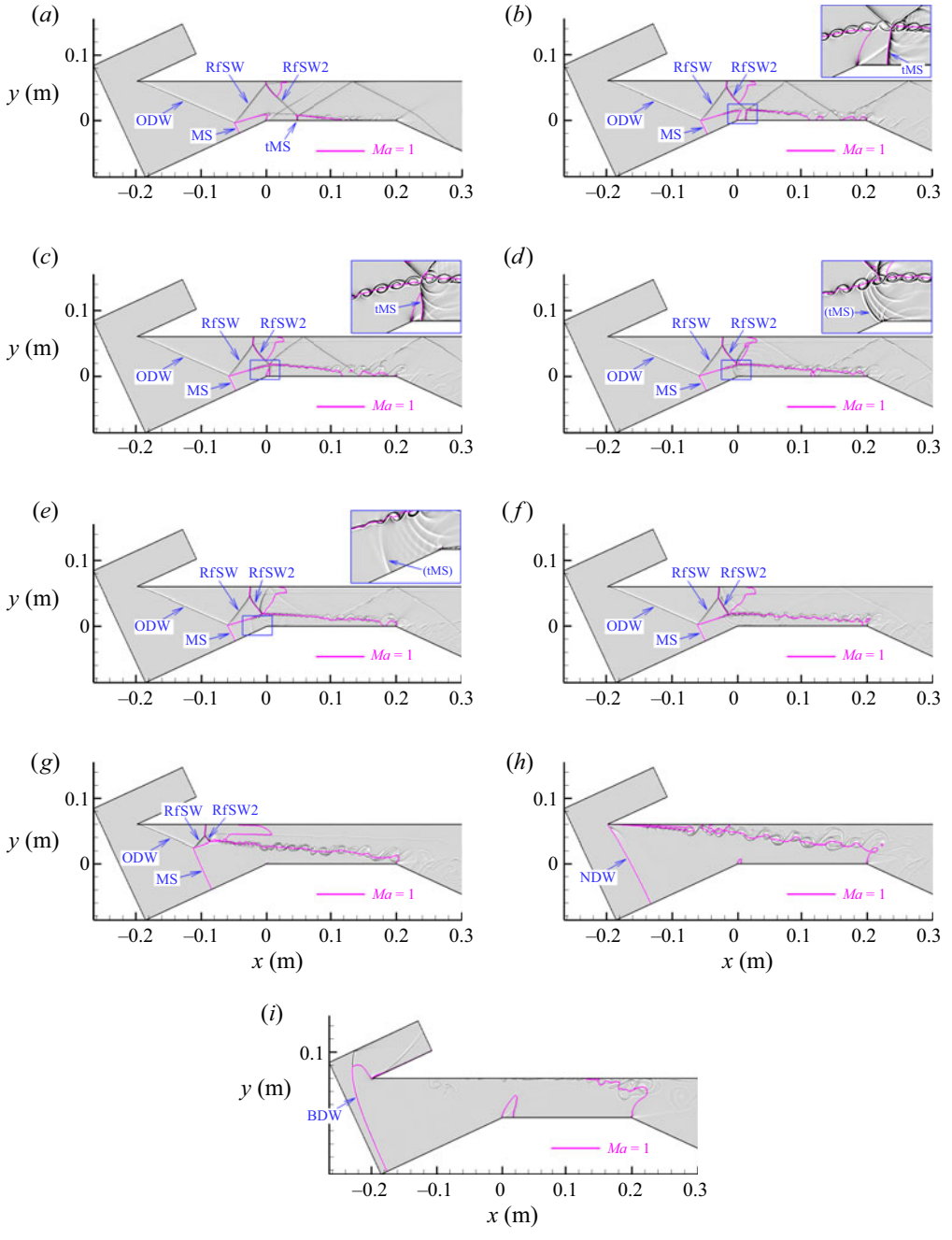

Figure 11. Shadowgraphs of the flow field of the destabilized Mach reflection of an ODW ($Ma = 10$, $\zeta = 30/60$) at different time instants: (*a*) $t = 0.369$ ms, (*b*) $t = 0.534$ ms, (*c*) $t = 0.585$ ms, (*d*) $t = 0.623$ ms, (*e*) $t = 0.665$ ms, (*f*) $t = 0.713$ ms, (*g*) $t = 1.080$ ms, (*h*) $t = 1.345$ ms and (*i*) $t = 1.582$ ms.

Taking $\zeta = 30/60$ as an example, the evolution of the flow field of the destabilized Mach reflection of an ODW at $Ma = 10$ is illustrated in figure 11 by shadowgraphs along with sonic lines. The time instants corresponding to the exhibited flow fields are also marked along the motion speed curve of the pressure-jump point in figure 10 for convenience.

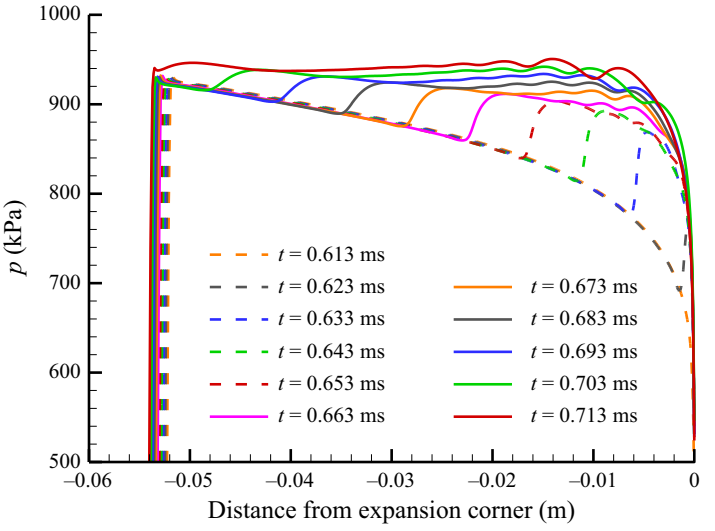

Figure 12. Pressure distributions along the wall before the expansion corner of the destabilized Mach reflection of an ODW ($Ma = 10$, $\zeta = 30/60$) at different time instants.

After the Mach reflection pattern of the ODW is established (figure 11*a*), flow structures similar to the stabilized structures in § 3.2, including the MS, SL, RfSW, RfSW2, tMS and subsonic zone, also appear in the flow field of this destabilized case. In the early period of evolution of this destabilized Mach reflection of the ODW, the tMS is located relatively far downstream from the subsonic zone behind the MS (figure 11*a*). As time proceeds, the upstream motion of the MS drives the following flow structures (e.g. the RfSW, RfSW2 and tMS) upstream; consequently, the location of the tMS approaches the subsonic zone behind the MS (figure 11*b*). As indicated in figure 10(*a*), the flow structures tend to stabilize since the motion speed decreases to zero during this period. However, at approximately $t = 0.585$ ms (figure 11*c*), the tMS acts on the subsonic zone before the flow structures are fully stabilized. Thereafter, the pressure rise caused by the tMS rapidly propagates upstream through this subsonic zone, as shown in figures 11(*d*) and 11(*e*). Note that the symbol 'tMS' in these two figure panels is enclosed in parentheses, implying that the pressure rise caused by the tMS is no longer as sharp as that of a shock wave due to the diffusion effects of propagating through a subsonic zone.

The upstream propagation of the pressure rise caused by the tMS is also clearly visualized in figure 12, showing the evolution of the pressure distributions along the wall before the expansion corner (after the tMS acts on the subsonic zone). As shown in figure 12, the pressure rise caused by the tMS propagates upstream through the subsonic zone and finally arrives at the detonation front of the MS at approximately $t = 0.713$ ms (see also figure 11*f*), resulting in an increase in the pressure behind the MS and consequently the pressure ratio across the MS. Notably, the pressure ratio across an overdriven detonation wave must match its propagation speed relative to the incoming flow, and vice versa. Therefore, this increase in the pressure ratio across the MS results in an increase in its relative propagation speed; that is, the MS accelerates while moving upstream, as indicated by the sudden increase in the motion speed of the MS (point 'f') in figure 10(*a*). Then, the upstream motion of the MS enters a so-called 'positive feedback' period: the more upstream the MS travels, the closer the distance between the MS and RfSW2 (figure 11*g*), the higher the pressure ratio across the MS induced by

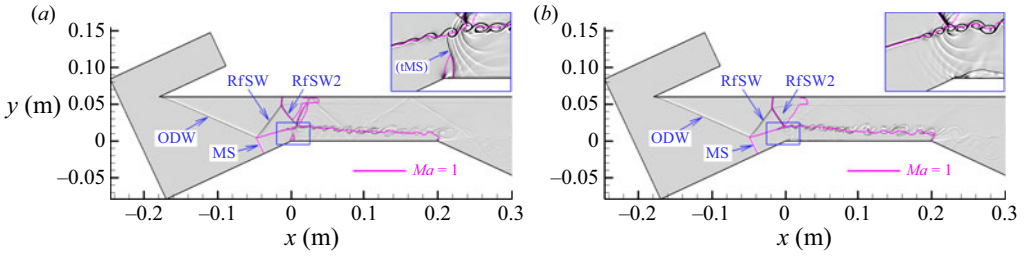

Figure 13. Shadowgraphs of the flow field of the destabilized Mach reflection of an ODW ($Ma = 10$, $\zeta = 20/60$) at different time instants: (*a*) $t = 0.826$ ms and (*b*) $t = 0.982$ ms.

the RfSW2 pressure rise and, consequently, the larger the upstream motion speed of the MS. As depicted in figure 10(*a*), the motion speed of the MS increases continuously and reaches a large value after the pressure rise produced by the tMS arrives at the detonation front. At approximately $t = 1.345$ ms (figure 11*h*), the MS reaches the leading tip of the cowl, and the ODW vanishes, resulting in only an NDW existing at the entrance of the combustor. Subsequently, the detonation front moves out of the combustor; instead, a bow detonation wave (BDW) forms and continues moving upstream, as shown in figure 11(*i*). In this destabilized case of the Mach reflection of an ODW ($Ma = 10$, $\zeta = 30/60$), because the detonation front that serves as the main combustion organization structure in the ODE moves out of the combustor and thereafter continues to move upstream with a large motion speed, the combustor (and thus the engine) cannot work normally and may even fail.

For $\zeta = 20/60$ at the same Ma, analyses of the instantaneous flow fields in combination with the evolutions of the MS location and its motion speed suggest that the sudden upstream acceleration of the MS during its apparent stabilization (figure 10*b*) can also be attributed to the action of the tMS on the subsonic zone behind the MS (as shown in figure 13), which causes a pressure rise that propagates upstream to the MS and subsequently results in the incompatibility of the pressure ratio across the MS and its relative propagation speed. Then, the upstream motion of the MS enters a positive feedback period, and the detonation front moves out of the combustor. At other flight Mach numbers (i.e. $Ma = 9.5$ and 10.5), destabilized Mach reflection patterns of ODWs also occur at large ζ values, as shown in figure 9, and similar analyses suggest that the relevant destabilization mechanisms are also similar. Since this kind of destabilization phenomenon is induced by the action of a shock wave (the tMS in this section), this process is referred to as wave-induced destabilization in this paper.

3.4. *Inherently destabilized Mach reflection of ODWs at low Ma*

As depicted in figure 9, for a relatively large Mach number ($Ma = 9.5$, 10 or 10.5), when the ζ (>0) value is small (i.e. the designed ODW reflection point is located close to the expansion corner), the flow structures of the Mach reflection of an ODW remain stabilized in the combustor, whereas the detonation front moves out of the combustor upstream for large ζ values (i.e. the designed ODW reflection point is located far upstream from the expansion corner), implying the destabilization of the Mach reflection pattern of the ODW. However, a special phenomenon of stabilization/destabilization occurs for a relatively low Mach number, for example $Ma = 9$, as shown in figure 14. For $Ma = 9$ and $\zeta = 12/60$, the Mach reflection of an ODW is destabilized in the combustor, and the evolution of the MS is similar to the evolutionary characteristics in the destabilized cases of $Ma = 10$. After the Mach reflection pattern of an ODW forms (corresponding to the first peak on the speed

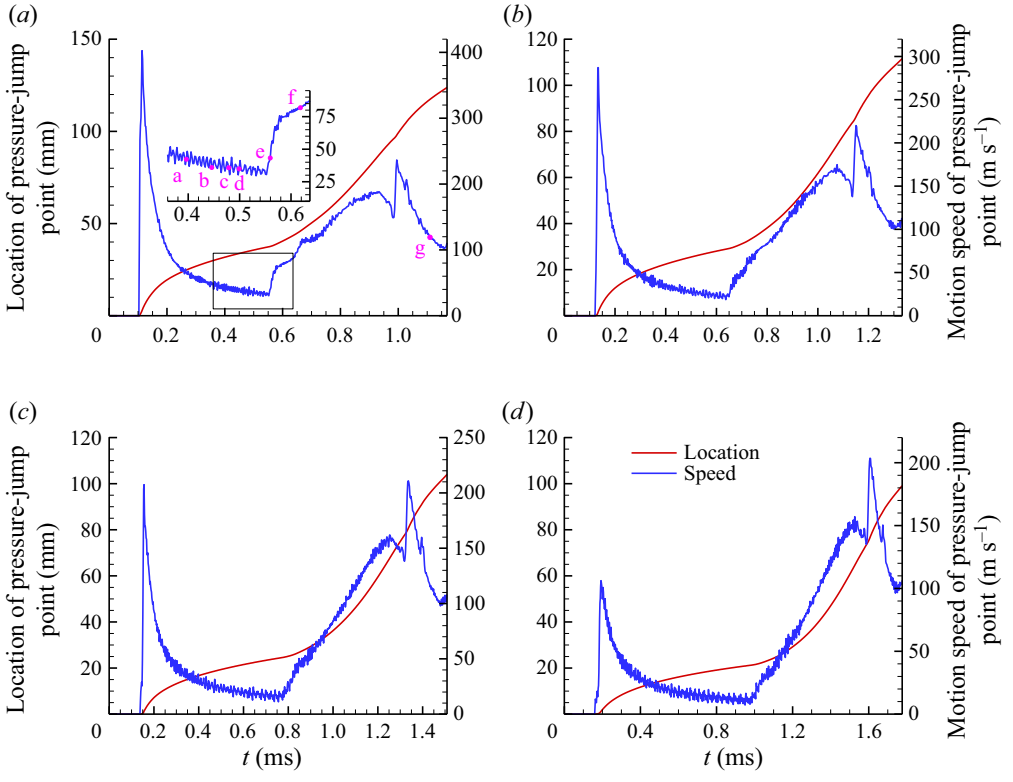

Figure 14. Evolutions of the location and corresponding motion speed of the pressure-jump point along the inlet wall of the destabilized Mach reflection of ODWs at $Ma = 9$: (*a*) $\zeta = 12/60$, (*b*) $\zeta = 6/60$, (*c*) $\zeta = 3/60$ and (*d*) $\zeta = 1/60$.

curve in figure 14*a* for this case), the upstream motion speed of the MS initially drops rapidly and then decreases gradually. During the stabilization of the MS, the motion speed of the MS suddenly rises, and the MS accelerates upstream. As a result, the MS moves out of the combustor to a location far upstream from the expansion corner. According to the previous analyses, one may expect to stabilize the Mach reflection of the ODW in the combustor by decreasing the ζ value, i.e. by setting the designed ODW reflection point closer to the expansion corner. However, while this guideline prevails for $Ma = 9.5$, 10 and 10.5, this solution fails for $Ma = 9$. By continuously decreasing the ζ value from 12/60 to 6/60, 3/60 or even 1/60, the motion speed of the MS still exhibits a sudden increase, eventually leading to the destabilization of the flow field. One of the key differences among the different ζ values is the time instant at which the motion speed of the MS rises; in other words, the time instant of the turning point occurs later for smaller ζ values. Notably, the designed reflection point is only 1 mm upstream of the expansion corner for a 6 cm high combustor with $\zeta = 1/60$, but the destabilization of the Mach reflection of an ODW still occurs for this extremely small value of ζ. Remarkably, the flow structures at this low Ma are stable with $\zeta = 0$, where the ODW reflects precisely at the expansion corner and the Mach reflection pattern of an ODW does not form. The above analyses suggest that destabilization is inherent in the Mach reflection of an ODW at this low Ma, when the ODW reflects off the wall before the expansion corner.

To determine the inherent mechanism causing the sudden increase in the motion speed of the MS in these low-Ma cases that directly destabilizes the Mach reflection of

ODWs, the instantaneous flow fields and pressure distributions along the wall before the expansion corner are analysed near the turning time instant, as shown in figures 15 and 16, respectively, taking $Ma = 9$ and $\zeta = 12/60$ as an example. Figure 15(*a*) demonstrates that the RfSW2 crosses the SL directly and then reflects off the lower wall at this low *Ma* rather than reflecting over the SL and forming a tMS at a relatively high *Ma* (e.g. figure 11*a*). Although slightly different flow structures are formed at this low *Ma*, the RfSW2 acts on the subsonic zone behind the MS at approximately $t = 0.446$ ms (figure 15*b*) as the MS moves upstream continuously. Thereafter, the pressure rise caused by the RfSW2 propagates upstream through this subsonic zone towards the detonation front of the MS, as shown in figures 15(*c–e*) and 16. After this pressure wave arrives at the detonation front of the MS at approximately $t = 0.560$ ms, the pressure behind the MS and the pressure ratio across the MS both increase; the resulting incompatibility between the pressure ratio across the MS and its relative propagation speed leads to a sudden increase in the motion speed of the MS (point 'e' in figure 14*a*), ultimately causing the destabilization of the detonation front in the combustor (figures 15*f* and 15*g*).

It is suggested that the Mach reflection of an ODW before an expansion corner ($\zeta > 0$) can be directly destabilized by the action of the RfSW2 or its tMS on the subsonic zone behind the MS regardless of the flight Mach number. Indeed, this is easy to understand with the above analyses. As the MS moves upstream, the RfSW2 and/or its tMS moves upstream and approaches the MS, and when the MS moves sufficiently far upstream from the expansion corner, the RfSW2 and/or its tMS acts on the subsonic zone and eventually causes destabilization. For a relatively high *Ma* (e.g. $Ma = 10$), the stabilized distance of the MS from the expansion corner increases as ζ increases. Consequently, a small ζ value results in a short distance of the MS from the expansion corner, which prevents the tMS of the RfSW2 from acting on the subsonic zone. On the other hand, a potentially long distance of the MS from the expansion corner is implied with a large ζ value, leading to destabilization. However, destabilization always occurs at $Ma = 9$, even with an extremely small ζ value of 1/60, implying that a stabilized MS location may not exist for this low Mach number and consequently that the MS may continuously move upstream once the Mach reflection pattern of the ODW forms. In other words, destabilization may be inherent in the Mach reflection of an ODW at a low *Ma*, and the action of the RfSW2 or its tMS on the subsonic zone behind the MS may only accelerate the upstream motion of the MS. Hence, this kind of destabilization phenomenon at a low *Ma* is referred to as inherent destabilization in this paper, and an in-depth theoretical analysis is further conducted to understand the relevant mechanisms.

3.5. *Formulating the stabilized location of the MS*

In the following formulation, the effects of the RfSW2 and its tMS are neglected since they are found to only accelerate the inherent upstream motion of the MS at a low *Ma*, as discussed in § 3.4. According to the above analyses of the instantaneous flow fields, the SL is inclined downward relative to the incoming flow, as is schematically shown in figure 17. Hence, the subsonic flow crossing the MS accelerates towards becoming sonic in the contracted flow path bounded by the SL and the lower wall, and the geometric throat is positioned at the expansion corner (point O). Assume that the MS is a straight line perpendicular to the lower wall and that the SL is also a straight line with an inclination angle of α relative to the incoming flow. According to the geometric relationship exhibited in figure 17, the length of the MS can be calculated by

$$\overline{\mathrm{MS}} = (\overline{\mathrm{MO}} - \overline{\mathrm{RO}}) \tan \beta, \tag{3.1}$$

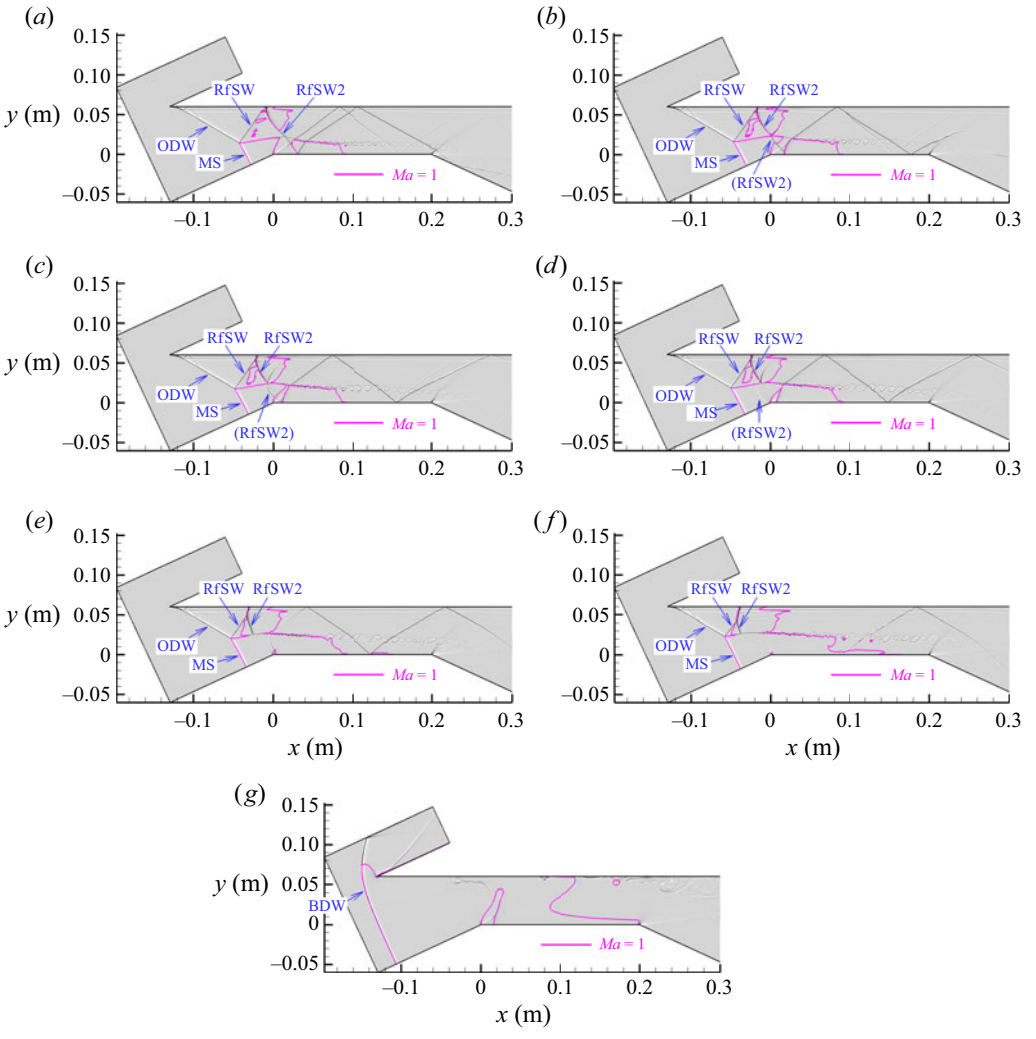

Figure 15. Shadowgraphs of the flow field of the destabilized Mach reflection of an ODW ($Ma = 9$, $\zeta = 12/60$) at different time instants: (*a*) $t = 0.396$ ms, (*b*) $t = 0.446$ ms, (*c*) $t = 0.479$ ms, (*d*) $t = 0.499$ ms, (*e*) $t = 0.560$ ms, (*f*) $t = 0.618$ ms and (*g*) $t = 1.110$ ms.

where β is the oblique detonation angle of the ODW relative to the incoming flow. The distance from the expansion corner to the SL, namely $\overline{\mathrm{OL}}$, which is considered as the width of the geometric throat, can be expressed as

$$\overline{\mathrm{OL}} = \overline{\mathrm{ON}}\cos\alpha = [(\overline{\mathrm{MO}} - \overline{\mathrm{RO}})\tan\beta - \overline{\mathrm{MO}}\tan\alpha]\cos\alpha, \tag{3.2}$$

where $\overline{\mathrm{ON}}$ is a segment parallel to MS. Therefore, the contraction ratio of the flow path from the MS to the geometric throat $\overline{\mathrm{OL}}$ appears as

$$\begin{aligned}\frac{\overline{\mathrm{MS}}}{\overline{\mathrm{OL}}} &= \frac{(\overline{\mathrm{MO}} - \overline{\mathrm{RO}})\tan\beta}{[(\overline{\mathrm{MO}} - \overline{\mathrm{RO}})\tan\beta - \overline{\mathrm{MO}}\tan\alpha]\cos\alpha} \\ &= \left\{\left[1 - \frac{\tan\alpha}{(1 - \overline{\mathrm{RO}}/\overline{\mathrm{MO}})\tan\beta}\right]\cos\alpha\right\}^{-1}.\end{aligned} \tag{3.3}$$

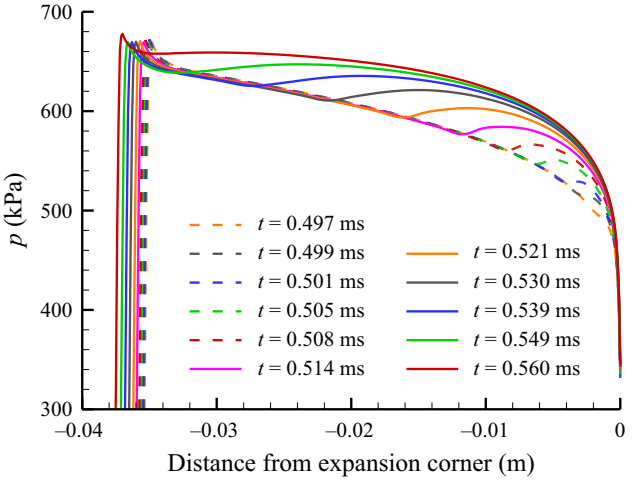

Figure 16. Pressure distributions along the wall before the expansion corner of the destabilized Mach reflection of an ODW ($Ma = 9$, $\zeta = 12/60$) at different time instants.

Equation (3.3) reveals that as the S point (the triple point) of the MS moves upstream along the ODW (i.e. the triple point is always located on the ODW), the ratio of $\overline{\mathrm{RO}}/\overline{\mathrm{MO}}$ (<1) decreases, and the contraction ratio of the flow path, $\overline{\mathrm{MS}}/\overline{\mathrm{OL}}$, decreases accordingly. If the MS is located close to the expansion corner, the contraction ratio of the flow path behind the MS is large enough that a sonic state may be achieved before the geometric throat $\overline{\mathrm{OL}}$, as schematically shown in figure 17(a) (the location of the carmine dashed line corresponds to the contraction ratio of the flow path of the sonic state). Notably, the streamlines behind the MS are generally curved to adjust the flow direction to conform to the flow path between the SL and the lower wall. Further contraction of the flow path behind the sonic line would directly choke the flow. As a result, the MS would move upstream to adjust the flow behind the MS to ensure that the sonic state occurs at the geometric throat $\overline{\mathrm{OL}}$. Obviously, the geometric converging effects of the flow path before the expansion corner contribute to sustaining the MS. In contrast, if the MS is located far upstream from the expansion corner (figure 17b), the contraction ratio becomes so small that the local Mach number at the geometric throat $\overline{\mathrm{OL}}$ is still smaller than one. In other words, under this circumstance, the flow behind the MS may be subsonic throughout the flow path before and across the expansion corner. Then, the geometric diverging effects of the flow path behind the expansion corner could propagate upstream through left-running characteristic lines across the expansion corner and arrive at the MS, which weakens the geometric converging effects of the flow path before the expansion corner. As a result, the MS would be blown away by the upstream supersonic flow. It appears that the stabilized location of the MS (i.e. $\overline{\mathrm{MO}}$) corresponds to a critical condition in which the local Mach number at the geometric throat $\overline{\mathrm{OL}}$ is equal to one, which is similar to the Kantrowitz limit in the unstart problems of scramjet inlets (Curran & Murthy 2001). In such a problem, the Kantrowitz-limit contraction ratio is determined by the one-dimensional isentropic area ratio that accelerates a subsonic flow (behind a normal shock wave) to a sonic flow at the throat. In the present problem regarding the stabilization of the Mach reflection of an ODW, the similar Kantrowitz-limit contraction ratio, $CR_{Kantrowitz}$, can be evaluated for a specific NDW, and it can be employed to determine the theoretical stabilization location of the MS.

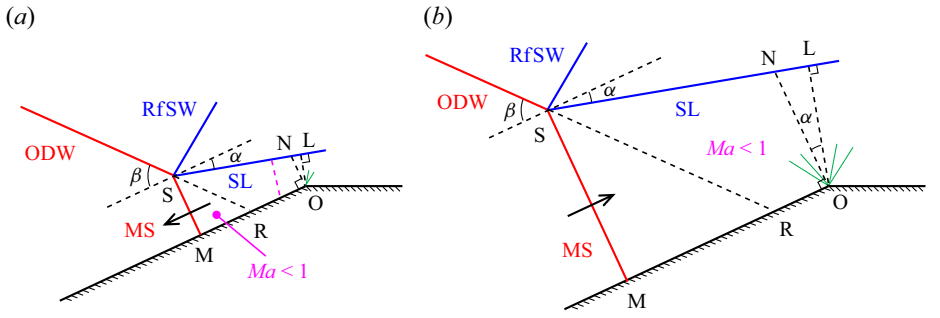

Figure 17. Geometric relationship of the Mach reflection of an ODW before an expansion corner: (*a*) $\overline{\mathrm{MS}}/\overline{\mathrm{OL}} > CR_{Kantrowitz}$ and (*b*) $\overline{\mathrm{MS}}/\overline{\mathrm{OL}} < CR_{Kantrowitz}$.

From the above analysis, the critical condition for the stabilization of the MS appears as

$$Ma|_{\overline{\mathrm{OL}}} = 1, \tag{3.4}$$

or

$$\frac{\overline{\mathrm{MS}}}{\overline{\mathrm{OL}}} = CR_{Kantrowitz}. \tag{3.5}$$

Substituting (3.3) into (3.5) yields the formula for calculating the stabilized location of the MS, expressed as

$$\frac{\overline{\mathrm{MO}}}{\overline{\mathrm{RO}}} = \frac{(\cos\alpha - CR_{Kantrowitz}^{-1})\tan\beta}{(\cos\alpha - CR_{Kantrowitz}^{-1})\tan\beta - \sin\alpha}. \tag{3.6}$$

Obviously, with the parameters α, β and $CR_{Kantrowitz}$ being known, the stabilized location of MS (i.e. $\overline{\mathrm{MO}}$) corresponding to the designed reflection location of ODW (i.e. $\overline{\mathrm{RO}}$) can be evaluated directly from (3.6).

To evaluate the oblique detonation angle of the ODW, β, the inclination angle of the SL, α, and the Kantrowitz-limit contraction ratio behind the MS, $CR_{Kantrowitz}$, for different cases, the chemical equilibrium hypothesis is employed in the present study to account for changes in the chemical compositions and gas thermodynamic properties and to more accurately predict the heats of chemical reactions; that is, the chemical reaction rates are assumed to be infinitely fast, and chemical equilibrium states are assumed to be achieved everywhere in the flow field behind the leading shock/detonation fronts (i.e. behind the ODW and MS). Further, a two-step cyclic iterative solution method proposed by the authors (Zhang 2020*a*; Zhang *et al.* 2021*a*) is adopted to solve the chemical equilibrium solutions of different processes with high accuracy, including the chemical equilibrium normal shock relationship, the chemical equilibrium strong and weak oblique shock relationships (where 'strong' and 'weak' refer to the strong and weak branches of the oblique shock solutions, respectively) and the chemical equilibrium isentropic relationship. For clarity, the solution processes of the above chemical equilibrium relationships are briefly presented in Appendices A–E; for the detailed derivations and evaluations of the solution accuracy, the reader may refer to Zhang (2020*a*) and Zhang *et al.* (2021*a*). Specifically, for different cases, the oblique detonation angle of the ODW, β, can be directly evaluated by the chemical equilibrium weak oblique shock relationship; the predicted values of β in different cases agree well with those observed in the numerical simulations in the present study. For the evaluation of the Kantrowitz-limit contraction

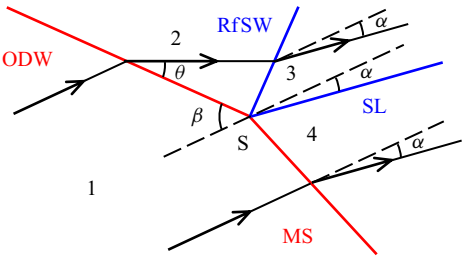

Figure 18. Illustration of the flows in the neighbourhood of the triple point of a Mach reflection pattern.

ratio behind the MS, $CR_{Kantrowitz}$, the flow state behind the MS is first obtained through the chemical equilibrium normal shock relationship; then, to evaluate the MS–throat area ratio through the chemical equilibrium isentropic relationship, the subsonic flow state needs to accelerate to the sonic state in the contracted flow path between the SL and the lower wall, during which the chemical compositions change due to shifts in chemical equilibrium. Moreover, to determine the inclination angle of the SL, α, the three-shock theory (Ben-Dor 2007) is applied to the neighbourhood of the triple point, as schematically shown in figure 18. The MS is slightly inclined with respect to the perpendicular direction of the incoming flow in the neighbourhood of the triple point S, and hence the flow state behind this small segment of the MS needs to be evaluated through the chemical equilibrium strong oblique shock relationship, while the change in the flow state across the RfSW (from region 2 to region 3, also based on the assumption of chemical equilibrium) is calculated by the chemical equilibrium weak oblique shock relationship. Thereafter, to determine the inclination angle of the SL, α, the pressure balance between both sides of the SL, namely between region 3 behind the RfSW that deflects the flow by an angle of $\theta - \alpha$ ($\theta = 25°$ in this paper) and region 4 behind the inclined MS that deflects the flow by an angle of α, i.e. $p_3 = p_4$ (figure 18), needs to be satisfied. With the chemical equilibrium strong and weak shock relationships, this pressure-balanced state can be solved by utilizing a simple dichotomizing search algorithm.

From the above analyses, the parameters α, β and $CR_{Kantrowitz}$ can be uniquely determined (based on the assumption of chemical equilibrium) according to the inflow conditions before the combustor, which depend uniquely on Ma, as shown in figure 19. The specific values of these parameters for the stabilized flight Mach numbers (i.e. $Ma = 9.5$, 10 and 10.5) are summarized in table 2. As Ma decreases, both the chemical equilibrium inclination angle of the SL, α, and the chemical equilibrium oblique detonation angle of the ODW, β, increase, whereas the chemical equilibrium Kantrowitz-limit contraction ratio behind the MS, $CR_{Kantrowitz}$, decreases. Because the flow Mach number behind the chemical equilibrium MS is closer to one at a lower Ma, it is easier for this subsonic flow to accelerate to the sonic state, leading to a smaller limiting contraction ratio. Substituting these parameters into (3.6), the predicted stabilized locations of the MS (i.e. $\overline{\mathrm{MO}}$) at $Ma = 9.5$, 10 and 10.5 as a function of the designed ODW reflection location (i.e. $\overline{\mathrm{RO}}$) are plotted as the dashed lines in figure 20. For comparison, the real values of $\overline{\mathrm{MO}}$ observed in the numerical simulations are also presented in figure 20, revealing that (3.6) underestimates the stabilized locations of the MS to a large extent compared with the numerical simulations.

These discrepancies in the stabilized locations of the MS between the theoretical predictions by (3.6) and the real observations via numerical simulations result from the following factors. First, the real SL between the triple point and the geometric throat is

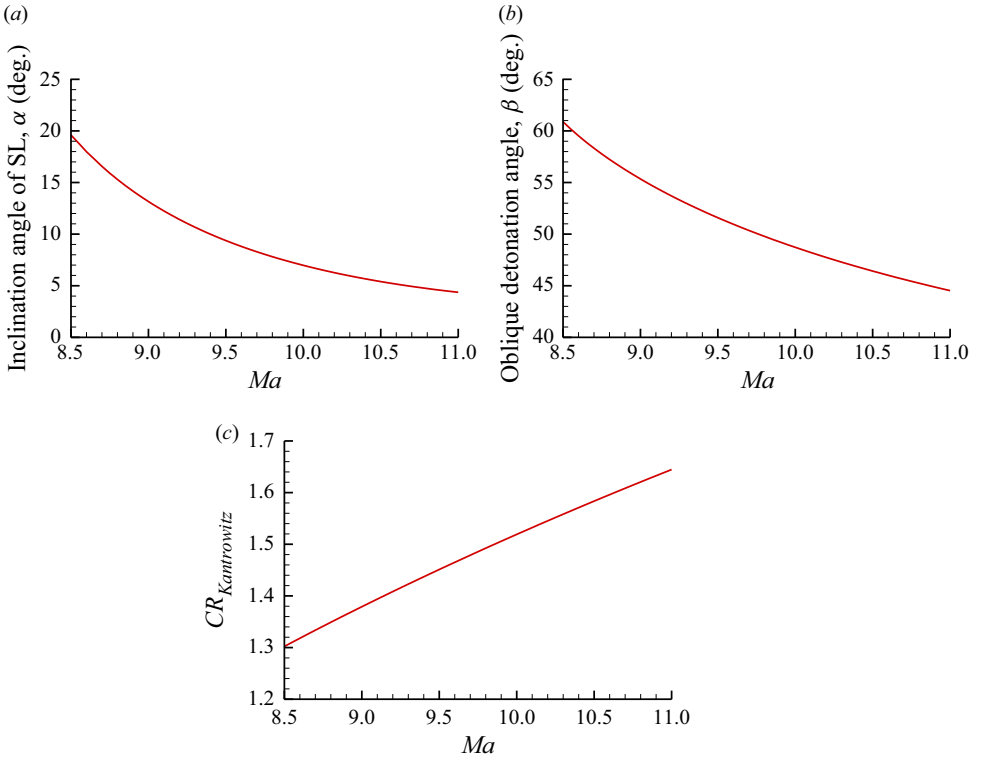

Figure 19. Changes in (*a*) the inclination angle of the SL, α, (*b*) the oblique detonation angle of the ODW, β, and (*c*) the Kantrowitz-limit contraction ratio behind the MS, $CR_{Kantrowitz}$, as functions of Ma based on the chemical equilibrium hypothesis.

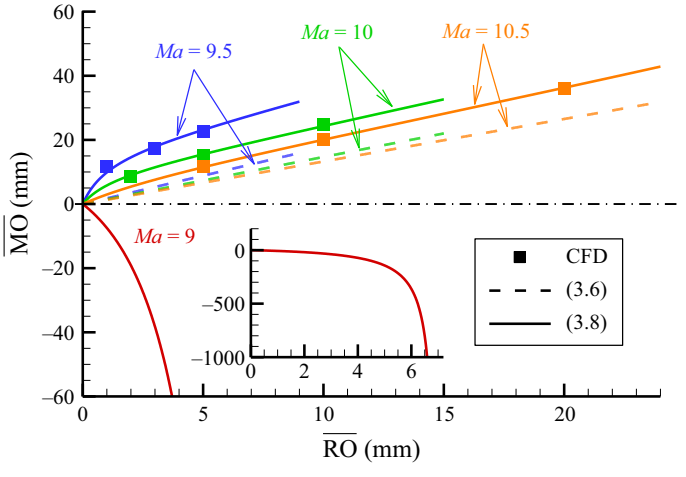

Figure 20. Changes in the stabilized location of the MS (i.e. $\overline{\mathrm{MO}}$) as a function of the designed ODW reflection location (i.e. $\overline{\mathrm{RO}}$).

not strictly straight, as shown in figure 21(*a*) (taking the case of $Ma = 10$ and $\zeta = 5/60$ as an example). Due to the limited space in the neighbourhood of the triple point compared with the chemical reaction characteristic length, the chemical equilibrium state is not fully achieved near the triple point, resulting in the local inclination angle of the SL being larger

Ma	ζ	$\overline{\mathrm{RO}}$ (mm)	$\overline{\mathrm{MO}}$ (mm)	α (deg.)	β (deg.)	$CR_{Kantrowitz}$	κ
9.5	1/60	1	11.64	9.38	51.59	1.4511	1.2267
9.5	3/60	3	17.26	9.38	51.59	1.4511	1.2049
9.5	5/60	5	22.60	9.38	51.59	1.4511	1.1911
10	2/60	2	8.73	6.97	48.72	1.5191	1.2980
10	5/60	5	15.00	6.97	48.72	1.5191	1.2651
10	10/60	10	24.84	6.97	48.72	1.5191	1.2370
10.5	5/60	5	11.60	5.40	46.42	1.5835	1.3272
10.5	10/60	10	19.97	5.40	46.42	1.5835	1.2924
10.5	20/60	20	36.18	5.40	46.42	1.5835	1.2594

Table 2. Summary of the geometric parameters in the stabilized Mach reflection of ODWs.

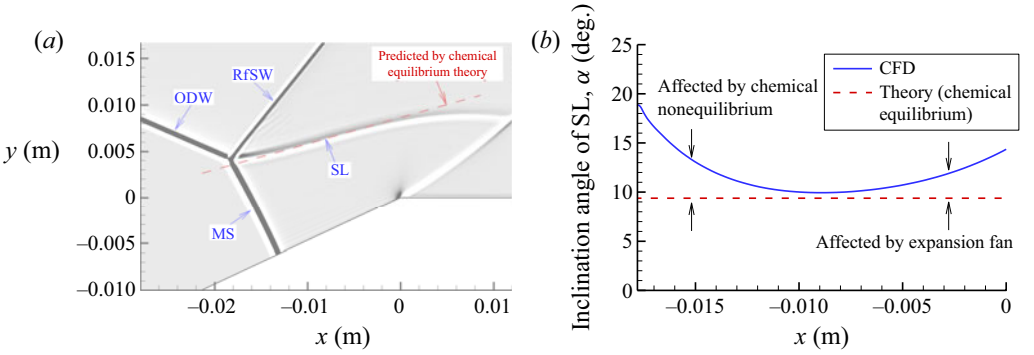

Figure 21. Numerical shadowgraph of the flow field near the reflection point of the ODW (a) and the spatial distribution of the local inclination angle of the SL (b) in the case of $Ma = 10$ and $\zeta = 5/60$.

than the corresponding chemical equilibrium value, as depicted in figure 21(b). As the fluid flows downstream, the flow state varies to the chemical equilibrium state, and hence the local inclination angle of the SL decreases gradually to the corresponding chemical equilibrium value. However, the segment of the SL close to the geometric throat $\overline{\mathrm{OL}}$ becomes increasingly inclined downward under the effects of the expansion fan emitted from the expansion corner (figure 21a), leading to an increase in the local inclination angle of the SL and another deviation from its chemical equilibrium value (figure 21b). Influenced by these two effects, the average inclination angle of the SL from the triple point to the geometric throat is undoubtedly larger than that predicted by the chemical equilibrium theory. Second, due to the local chemical non-equilibrium effects of the flow behind the MS, the change in the flow from the MS to the throat does not exactly follow the chemical equilibrium isentropic process. Furthermore, due to the special one-sided expansion geometry of the expansion corner and the finite-length contracted flow path in the present problem, the one-dimensional assumption in the traditional Kantrowitz limit is no longer satisfied (Curran & Murthy 2001), and hence the flow at the geometric throat $\overline{\mathrm{OL}}$ is not exactly at the sonic state; in fact, the Mach number of this flow is smaller than one and varies along $\overline{\mathrm{OL}}$, as shown, for example, in figures 4(g) and 8. As a result, the real contraction ratio from the MS to the geometric throat $\overline{\mathrm{OL}}$, i.e. $\overline{\mathrm{MS}}/\overline{\mathrm{OL}}$, deviates slightly from the chemical equilibrium Kantrowitz-limit contraction ratio, $CR_{Kantrowitz}$.

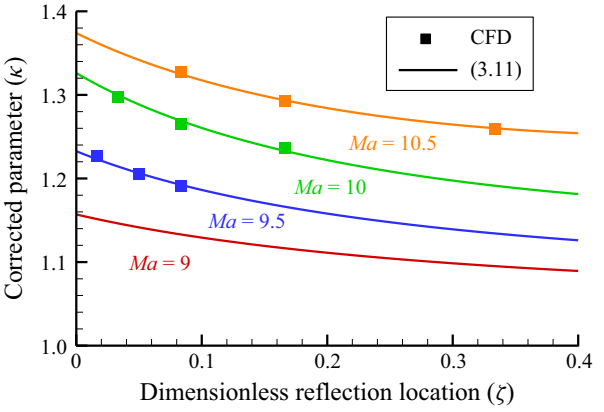

Figure 22. Changes in the corrected parameter, κ, as a function of the dimensionless reflection location, ζ.

To consider the above factors causing the discrepancies in the theoretical predictions of the stabilized locations of the MS compared to the numerical observations, a corrected parameter, κ, is introduced to the present theoretical formulation, and the critical condition for the stabilization of the MS, i.e. (3.5), is rewritten as

$$\kappa \frac{\overline{\mathrm{MS}}}{\overline{\mathrm{OL}}} = CR_{Kantrowitz}. \tag{3.7}$$

Then, a corrected formula for calculating the stabilized location of the MS is obtained by substituting (3.3) into (3.7), expressed as

$$\frac{\overline{\mathrm{MO}}}{\overline{\mathrm{RO}}} = \frac{(\cos\alpha - \kappa CR^{-1}_{Kantrowitz})\tan\beta}{(\cos\alpha - \kappa CR^{-1}_{Kantrowitz})\tan\beta - \sin\alpha}. \tag{3.8}$$

To evaluate the corrected parameter, κ, (3.8) is rearranged into

$$\kappa = \left[\cos\alpha - \frac{\sin\alpha}{(1 - \overline{\mathrm{RO}}/\overline{\mathrm{MO}})\tan\beta}\right] CR_{Kantrowitz}, \tag{3.9}$$

which is substituted with the numerical values of $\overline{\mathrm{MO}}$ in the stabilized cases at $Ma = 9.5$, 10 and 10.5 summarized in table 2. The value of κ ranges from approximately 1.19 to 1.33 for these stabilized Mach reflection cases. Although the corrected parameter, κ, does not change much between different cases, it appears to be a function of the flight Mach number, Ma, and the dimensionless reflection location, ζ, i.e. $\kappa = \kappa(Ma, \zeta)$, as depicted in figure 22.

One purpose of this section is to provide theoretical predictions of the stabilized locations of the MS at $Ma = 9$ and small ζ values, especially its asymptotic behaviour as ζ goes to zero at this relatively low Ma. Since the values of Ma and ζ do not change much compared to those in the stabilized cases summarized in table 2, a second-order Taylor expansion approximation of the function of $f(Ma, \zeta) \equiv (\kappa - 1)^{-1}$ can be applied to fit the corrected parameter, κ, as follows:

$$\begin{aligned}(\kappa - 1)^{-1} = f(Ma, \zeta) \approx f_0 &+ \frac{\partial f}{\partial Ma}(Ma - Ma_0) + \frac{\partial f}{\partial \zeta}(\zeta - \zeta_0) + \frac{\partial^2 f}{\partial Ma^2}(Ma - Ma_0)^2 \\ &+ \frac{\partial^2 f}{\partial \zeta^2}(\zeta - \zeta_0)^2 + \frac{\partial^2 f}{\partial Ma \partial \zeta}(Ma - Ma_0)(\zeta - \zeta_0).\end{aligned} \tag{3.10}$$

After rearranging the above equation, it can be rewritten as

$$\kappa(Ma, \zeta) = 1 + (a_1 + a_2 Ma + a_3 \zeta + a_4 Ma^2 + a_5 \zeta^2 + a_6 Ma\zeta)^{-1}, \tag{3.11}$$

where $a_1 = 187.3$, $a_2 = -35.23$, $a_3 = 67.63$, $a_4 = 1.680$, $a_5 = -5.364$ and $a_6 = -5.937$, as determined by the least squares method using the data of κ given in table 2. The fitting curves of $\kappa = \kappa(Ma, \zeta)$ by (3.11) are presented in figure 22. The fitting curves and the numerical data of the stabilized cases exhibit good agreement. Further, the corrected theoretical predictions of the stabilized locations of the MS (i.e. $\overline{\mathrm{MO}}$) using (3.8) and (3.11) are also presented in figure 20 as the solid lines, demonstrating good consistency between the corrected theoretical predictions and the numerical observations of the stabilized cases.

For $Ma = 9$, the chemical equilibrium oblique detonation angle of the ODW and the inclination angle of the SL are $\beta = 55.34°$ and $\alpha = 13.16°$, respectively, while the corresponding chemical equilibrium Kantrowitz-limit contraction ratio of the subsonic flow behind the MS is $CR_{Kantrowitz} = 1.3790$. For $\zeta = 1/60$ (i.e. $\overline{\mathrm{RO}} = 1$ mm), the predicted value of the corrected parameter using (3.11) is $\kappa = 1.151$. Substituting all the above parameters into (3.8), the theoretical prediction of the ratio of $\overline{\mathrm{MO}}/\overline{\mathrm{RO}}$ is equal to -7.454, which is smaller than zero. This result obviously contradicts the geometric relationship depicted in figure 17, i.e. $\overline{\mathrm{MO}}/\overline{\mathrm{RO}} > 1 > 0$, implying that a stabilized location of the MS (i.e. $\overline{\mathrm{MO}}$) cannot be achieved in this low-Ma case. Figure 23 shows the changes in the value of $\kappa\overline{\mathrm{MS}}/\overline{\mathrm{OL}}$–$CR_{Kantrowitz}$ as the MS moves upstream at $\zeta = 1/60$ (i.e. $\overline{\mathrm{RO}} = 1$ mm) for different Ma, revealing that the value of $\kappa\overline{\mathrm{MS}}/\overline{\mathrm{OL}}$–$CR_{Kantrowitz}$ is greater than zero when $\overline{\mathrm{MO}}$ is small for all Ma. According to the previous analysis of figure 17 but with the corrected critical condition of (3.7), when $\kappa\overline{\mathrm{MS}}/\overline{\mathrm{OL}}$–$CR_{Kantrowitz} > 0$, the flow becomes choked in the contracted flow path bounded by the SL and the lower wall, resulting in the MS moving upstream. In the cases of $Ma = 9.5$, 10 and 10.5, $\kappa\overline{\mathrm{MS}}/\overline{\mathrm{OL}}$–$CR_{Kantrowitz}$ approaches its zero point as $\overline{\mathrm{MO}}$ increases, and, finally, the MS remains stabilized at the corresponding location. In contrast, if the change in $\kappa\overline{\mathrm{MS}}/\overline{\mathrm{OL}}$–$CR_{Kantrowitz}$ passes through its zero point to a negative value in the cases of low Ma ($Ma = 9.5$, 10 and 10.5), the MS becomes attenuated downstream under the geometric diverging effects of the expansion corner; as a result, $\kappa\overline{\mathrm{MS}}/\overline{\mathrm{OL}}$–$CR_{Kantrowitz}$ returns to its zero point, and the MS remains stabilized. Therefore, the existence of zero points of $\kappa\overline{\mathrm{MS}}/\overline{\mathrm{OL}}$–$CR_{Kantrowitz}$ for these Ma values implies the potential stabilization of the MS at a specific location. However, the value of $\kappa\overline{\mathrm{MS}}/\overline{\mathrm{OL}}$–$CR_{Kantrowitz}$ is always greater than zero, and there is no zero point in the evolution of $\overline{\mathrm{MO}}$ in the case of $Ma = 9$. Therefore, the MS grows and moves upstream continuously after it forms, leading to the destabilization of the Mach reflection of the ODW in this low-Ma case. Further, as depicted in figure 20, the predicted stabilized location of the MS at $Ma = 9$ is always negative for $\zeta > 0$, implying that the Mach reflection of ODWs is inherently destabilized at this low Ma due to flow choking, when the ODW reflects before an expansion corner, i.e. $\zeta > 0$, as discussed in § 3.4.

According to the previous analyses, the stabilization of the Mach reflection of an ODW before an expansion corner is feasible at small ζ because destabilization would be directly triggered by the action of the RfSW2 or its tMS on the subsonic zone behind the MS at large ζ. Due to the limited spatial resolution of numerical simulations, it is impossible to infinitely decrease ζ to check whether the Mach reflection of ODWs before an expansion corner at a specific Ma is inherently destabilized. However, the inherent stabilization or destabilization characteristics at a specific Ma can be confirmed by the asymptotic behaviour of $\overline{\mathrm{MO}}/\overline{\mathrm{RO}}$ when $\zeta \to 0+$, as shown in figure 24. The limit of $\overline{\mathrm{MO}}/\overline{\mathrm{RO}}$ is greater than zero when Ma is greater than approximately 9.3, implying that when ζ is

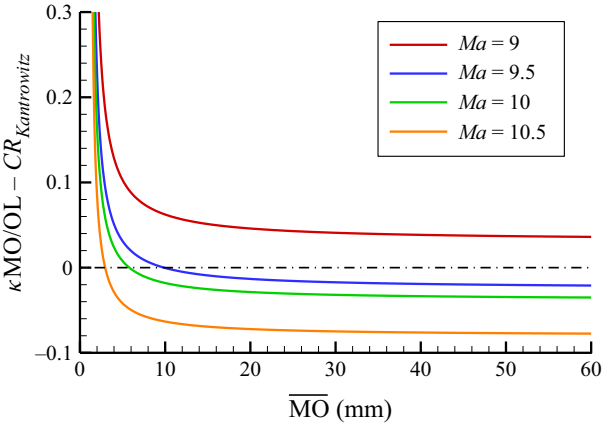

Figure 23. Changes in the value of $\kappa\overline{\mathrm{MS}}/\overline{\mathrm{OL}}$–$CR_{Kantrowitz}$ as a function of $\overline{\mathrm{MO}}$ for $\overline{\mathrm{RO}} = 1$ mm (i.e. $\zeta = 1/60$) at different *Ma*.

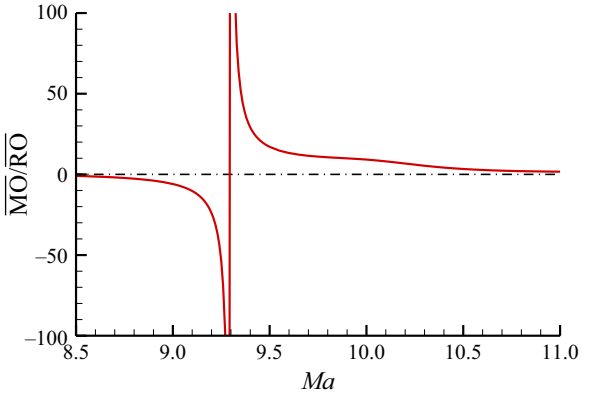

Figure 24. Asymptotic change in the value of $\overline{\mathrm{MO}}/\overline{\mathrm{RO}}$ as a function of *Ma* when $\overline{\mathrm{RO}} \to 0+$ (or $\zeta \to 0+$).

small enough that the RfSW2 or its tMS does not act on the subsonic zone behind the MS, the Mach reflection of an ODW before the expansion corner can be stabilized. For *Ma* smaller than approximately 9.3, the limit of $\overline{\mathrm{MO}}/\overline{\mathrm{RO}}$ is smaller than zero, implying that the Mach reflection of an ODW before an expansion corner is inherently destabilized regardless of how small ζ (>0) is. In other words, the critical Mach number of inherently stabilized/destabilized Mach reflection of ODWs before an expansion corner, Ma_{cri}, predicted by the present theory, is approximately 9.3. The present theoretical prediction is consistent with the numerical observations summarized in figure 9, in which the Mach reflections of ODWs can be stabilized with a small ζ at $Ma \geq 9.5$ but exhibit destabilization with all $\zeta > 0$ at $Ma = 9$. The numerical prediction of Ma_{cri} appears between 9 and 9.5.

Further, figure 19 shows that as *Ma* decreases, the inclination angle of the SL, α, increases, resulting in an increase in the real contraction extent of the flow path bounded by the SL and the lower wall, whereas the corresponding Kantrowitz-limit contraction ratio of the subsonic flow behind the MS decreases. Hence, the subsonic flow behind the MS is easily choked before the expansion corner at a low *Ma*. In other words, this subsonic flow may accelerate to the sonic state before the expansion corner and be choked by further area contraction, resulting in the MS continuously moving upstream and inherent

destabilization, as shown in figure 17(*a*). In summary, the theoretical results presented in this section demonstrate that the inherent destabilization of the Mach reflection of an ODW before an expansion corner at a low *Ma* is attributed to the geometric flow choking phenomenon caused by the large flow path contraction behind the MS.

4. Conclusions

In this paper, the inviscid Mach reflection patterns of ODWs before an expansion corner in a space-confined ODE combustor are numerically studied by solving the two-dimensional time-dependent multispecies reactive Euler equations in combination with a detailed hydrogen combustion mechanism. The effects of different flight Mach numbers (*Ma*) and different dimensionless reflection locations ($\zeta \geq 0$) on the stabilization/destabilization characteristics of the flow structures in the combustor and the relevant mechanisms are emphasized. The results suggest that a stabilized regular reflection pattern occurs at all *Ma* values when the ODW reflects precisely at the expansion corner, i.e. $\zeta = 0$. However, if the ODW reflects upstream of the expansion corner, i.e. $\zeta > 0$, a Mach reflection pattern emerges, and complex flow structures, such as the MS, SL, RfSW, RfSW2 and subsonic zone behind the MS, form in the combustor. The stabilization/destabilization characteristics of these formed flow structures in the Mach reflection pattern of the ODW depend on the values of *Ma* and ζ.

When *Ma* is not very low, e.g. $Ma = 9.5$, 10 and 10.5, and the ζ value is small (>0), the flow structures of the Mach reflection of the ODW remain stabilized in the combustor. Under this circumstance, the stabilized location of the MS and the downstream flow structures move upstream as ζ increases. In particular, the distance between the RfSW2 or its tMS and the subsonic zone behind the MS closes with increasing ζ. Further, when ζ increases beyond a specific value, wave-induced destabilization emerges. The RfSW2 or its tMS acts on the subsonic zone behind the MS, and the relevant pressure rise propagates through this subsonic zone towards the detonation front of the MS, leading to sudden increases in the pressure behind the MS and the pressure ratio across the MS. Although the upstream motion of the MS is seemingly stabilized initially, the incompatibility of the pressure ratio across the MS and its propagation speed relative to the incoming flow causes the MS to suddenly accelerate upstream. Then, the upstream motion of the MS enters a positive feedback stage, and its upstream motion speed continuously increases. Finally, the detonation front of the ODW vanishes, and the MS moves out of the combustor, resulting in the destabilization of the Mach reflection of the ODW at this large ζ value.

For a low *Ma*, for example $Ma = 9$, the Mach reflection patterns of ODWs are destabilized at any $\zeta > 0$ (even as small as $\zeta = 1/60$), implying inherent destabilization, although the reflection flow field of an ODW is stabilized at $\zeta = 0$ at this low *Ma* or at small $\zeta > 0$ at a higher *Ma*. Analyses of the evolution of the flow fields and pressure distributions reveal that the inherent destabilization of the Mach reflection of an ODW at a low *Ma* is also directly induced by the action of the RfSW2 or its tMS on the subsonic zone behind the MS during the inherently continuous upstream movement of the MS. Further analyses conducted by theoretically formulating the stabilized location of the MS suggest that its inherently continuous upstream motion and consequently the inherent destabilization of the flow field are attributed to choking of the flow in the contracted flow path between the SL and the lower wall at low *Ma* values, where the inclination angle of the SL relative to the incoming flow is large and hence the geometric contraction of the flow path is large.

The above results imply that inviscid destabilization of the flow field occurs easily when the ODW reflects off the wall before the expansion corner of the combustor, causing a Mach reflection pattern to form, which is unfavourable to the operation of an

ODE combustor because failure of the engine may occur. Therefore, this study clearly demonstrates that, to avoid the potential destabilization of the Mach reflection patterns of ODWs, the reflection point of the ODW should not be designed to be located before the expansion corner. Instead, the reflection point of the ODW should be designed downstream of the expansion corner, as suggested by the authors' previous research (Zhang *et al.* 2020*b*, 2021*b*), where the stabilized viscous flow fields of ODWs or ODW reflections were obtained, even for a low Ma (i.e. $Ma = 9$). Moreover, future studies can focus on (1) the effects of viscous factors, especially boundary layers and shock/detonation-induced boundary layer separations, on the stabilization characteristics of an ODW when the ODW is designed to reflect downstream of the expansion corner, (2) the relevant flow mechanisms and (3) the stabilization-control strategies in the engine combustor.

Funding. This work is supported by the National Natural Science Foundation of China (grant nos 11772284, 11672312 and 11532014).

Declaration of interests. The authors report no conflict of interest.

Author ORCIDs.
Zijian Zhang https://orcid.org/0000-0002-7656-2734;
Chihyung Wen https://orcid.org/0000-0002-1181-8786.

Appendix A. Two-step cyclic iterative solution method for different chemical equilibrium relationships

Problem description: the pressure p_1, temperature T_1, velocity u_1 and chemical compositions χ_{i1} (in molar fraction, $i = 1, \ldots, nSp$, where nSp is the number of species considered in the mixture) are known before a reactive normal shock wave or OSW or before starting an isentropic process; additionally, the deflection angle θ is known for the reactive oblique shock problem, or the target pressure p_2 is known for the isentropic process. By assuming infinite chemical reaction rates (i.e. chemical equilibrium), the pressure p_2 (except for the isentropic process), temperature T_2, velocity u_2, chemical compositions χ_{i2} and oblique shock angle β (only for an oblique shock) behind the reactive normal shock wave or OSW or after the isentropic process need to be solved.

The method adopted to solve the above chemical equilibrium relationships, namely the chemical equilibrium normal shock relationship, the chemical equilibrium strong or weak normal shock relationship and the chemical equilibrium isentropic relationship, is the two-step cyclic iterative solution method, which was previously proposed by the authors (Zhang 2020*a*; Zhang *et al.* 2021*a*). A flow diagram illustrating the solution process is presented in figure 25, where $\lambda = 0.4$ is a relaxation factor to ensure stability and convergence in the iteration process and k is an index of the iteration step. Moreover, the convergence criteria in figure 25 can be chosen as follows:

$$\text{Error} = \max\left\{\frac{|p_2^{(k+1)} - p_2^{(k)}|}{p_2^{(k+1)}}, \frac{|T_2^{(k+1)} - T_2^{(k)}|}{T_2^{(k+1)}}, |\chi_{i2}^{(*)} - \chi_{i2}^{(k)}|\right\} < 10^{-7}. \tag{A1}$$

For the calculation of the chemical equilibrium normal shock relationship, Step 1 in figure 25 is specified as the calculation of the multispecies normal shock relationship by giving p_1, T_1, u_1, χ_{i1} and χ_{i2}, and the detailed calculation process is given in Appendix B.

For the calculation of the chemical equilibrium strong or weak normal shock relationship, Step 1 in figure 25 is specified as the calculation of the multispecies strong

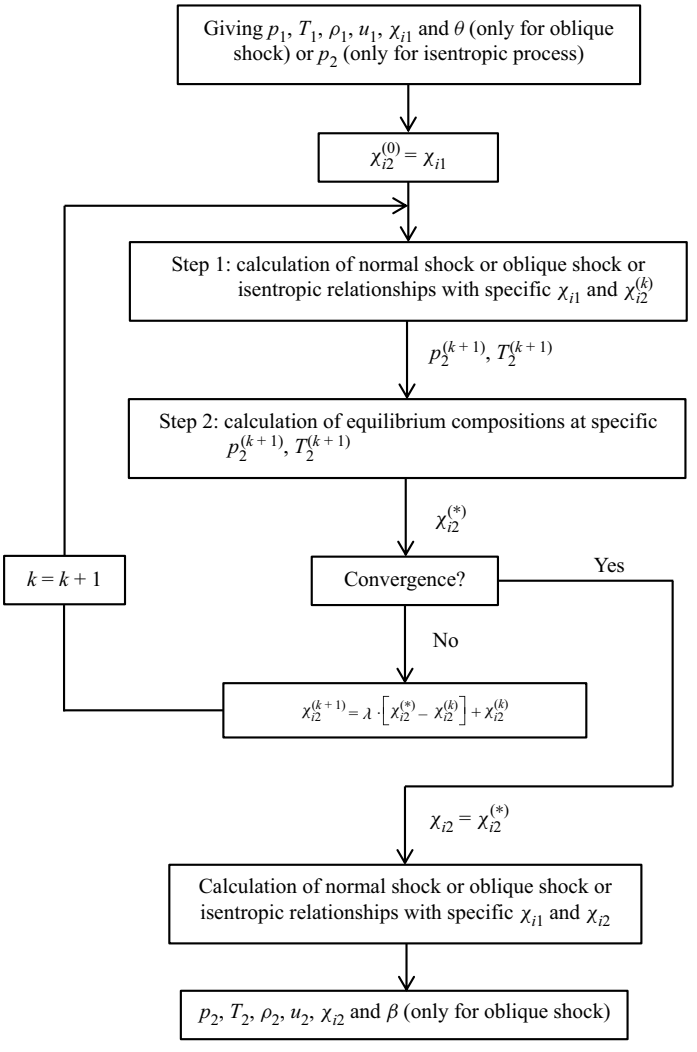

Figure 25. Diagram of the solution process of the two-step cyclic iterative solution method.

or weak oblique shock relationship by giving p_1, T_1, u_1, θ, χ_{i1} and χ_{i2}, and the detailed calculation process is given in Appendix C.

For the calculation of the chemical equilibrium isentropic relationship, Step 1 in figure 25 is specified as the calculation of the multispecies isentropic relationship by giving p_1, T_1, u_1, χ_{i1}, χ_{i2} and p_2, and the detailed calculation process is given in Appendix D.

For the calculations of all the above chemical equilibrium relationships, the determination of the chemical equilibrium compositions, χ_{i2}, at the given p_2 and T_2, i.e. Step 2 in figure 25, is given in Appendix E in detail.

Appendix B. Calculation of the normal shock relationship with varying compositions

Problem description: the pressure p_1, temperature T_1, velocity u_1 and chemical compositions χ_{i1} before a normal shock wave are known. Additionally, the chemical

compositions χ_{i2} behind the normal shock are also known, but they do not need to be the same as χ_{i1} to account for chemical reactions. Then, the post-shock pressure p_2, temperature T_2 and velocity u_2 are solved. A single-variable Newton iteration method derived from the governing equations of a normal shock wave is adopted here to solve the post-shock velocity u_2 (the iteration variable). The iteration function $f_{NSW}(u_2)$ is expressed as

$$\left.\begin{aligned} f_{NSW}(u_2) = f_{NSW}(u_2, T_2) = h_2(T_2) + \frac{1}{2}u_2^2 - h_1(T_1) - \frac{1}{2}u_1^2 = 0, \\ T_2(u_2) = \frac{u_2}{R_2}\left(\frac{R_1 T_1}{u_1} + u_1 - u_2\right), \end{aligned}\right\} \tag{B1}$$

where R_1 and R_2 are the gas constants of the mixtures before and behind the normal shock wave, respectively, and they can be easily calculated from the relevant chemical compositions of mixtures. Moreover, h_1 and h_2 are the specific enthalpies of the mixtures before and behind the normal shock wave, respectively, and they can be evaluated at the given temperature from a species thermodynamic database with known mixture compositions, for example, the piecewise fourth-order temperature polynomial fitting of NASA (McBride, Gordon & Reno 1993). The Newton iteration formula appears as

$$u_{2,k+1} = u_{2,k} - \frac{f_{NSW}(u_{2,k})}{f'_{NSW}(u_{2,k})}, \tag{B2}$$

where the initial iteration value can be set as $u_{2,0} = 0$. In (B2), the derivative of the iteration function, $f'_{NSW}(u_2)$, is expressed as

$$\left.\begin{aligned} f'_{NSW}(u_2) = \frac{c_{p2}(T_2)}{R_2}\left(\frac{R_1 T_1}{u_1} + u_1 - 2u_2\right) + u_2, \\ \frac{\mathrm{d}T_2}{\mathrm{d}u_2} = \frac{1}{R_2}\left(\frac{R_1 T_1}{u_1} + u_1 - 2u_2\right), \end{aligned}\right\} \tag{B3}$$

where c_{p2} is the specific heat at constant pressure of the mixture behind the normal shock wave. After calculating u_2, other unknown post-shock parameters can be obtained directly by substituting u_2 into the normal shock governing equations.

Appendix C. Calculation of the strong or weak oblique shock relationship with varying compositions

Problem description: the pressure p_1, temperature T_1, velocity u_1 and chemical compositions χ_{i1} before an OSW and the flow deflection angle θ across the oblique shock are known. Additionally, the chemical compositions χ_{i2} behind the oblique shock are also known, but they do not need to be the same as χ_{i1} to account for chemical reactions. Then, the post-shock pressure p_2, temperature T_2 and velocity u_2 and the oblique shock angle β are solved. A similar single-variable Newton iteration method derived from the governing equations of an oblique shock wave is also adopted. Here, the iteration variable is the oblique shock angle β, and the iteration function $f_{OSW}(\beta)$ appears as

$$\left.\begin{aligned} f_{OSW}(\beta) = f_{OSW}(\beta, u_{2n}, T_2) = h_2(T_2) + \frac{1}{2}u_{2n}^2 - h_1(T_1) + \frac{1}{2}u_1^2 \sin^2\beta = 0, \\ T_2(\beta, u_{2n}) = \frac{u_{2n}}{R_2}\left(\frac{R_1 T_1}{u_1 \sin\beta} + u_1 \sin\beta - u_{2n}\right), \\ u_{2n}(\beta) = u_1 \cos\beta \tan(\beta - \theta). \end{aligned}\right\} \tag{C1}$$

Then, the Newton iteration formula is

$$\beta_{k+1} = \beta_k - \frac{f_{OSW}(\beta_k)}{f'_{OSW}(\beta_k)}, \tag{C2}$$

with the derivative of the iteration function, $f'_{OSW}(\beta)$, expressed as

$$\left.\begin{aligned} f'_{OSW}(\beta) = \frac{\mathrm{d}f_{OSW}}{\mathrm{d}\beta} &= \frac{\partial f_{OSW}}{\partial \beta} + \frac{\partial f_{OSW}}{\partial u_{2n}} \cdot \frac{\mathrm{d}u_{2n}}{\mathrm{d}\beta} + \frac{\partial f_{OSW}}{\partial T_2}\left(\frac{\partial T_2}{\partial \beta} + \frac{\partial T_2}{\partial u_{2n}} \cdot \frac{\mathrm{d}u_{2n}}{\mathrm{d}\beta}\right), \\ \frac{\partial f_{OSW}}{\partial \beta} = -u_1^2 \sin\beta\cos\beta, \quad \frac{\partial f_{OSW}}{\partial u_{2n}} &= u_{2n}, \quad \frac{\partial f_{OSW}}{\partial T_2} = \frac{\mathrm{d}h_2(T_2)}{\mathrm{d}T_2} = c_{p2}(T_2), \\ \frac{\mathrm{d}u_{2n}}{\mathrm{d}\beta} &= u_1\left[\frac{\cos\beta}{\cos^2(\beta-\theta)} - \sin\beta\tan(\beta-\theta)\right], \\ \frac{\partial T_2}{\partial \beta} &= \frac{u_{2n}}{R_2}\left(u_1\cos\beta - \frac{RT_1}{u_1}\cdot\frac{\cos\beta}{\sin^2\beta}\right), \\ \frac{\partial T_2}{\partial u_{2n}} &= \frac{1}{R_2}\left(\frac{RT_1}{u_1\sin\beta} + u_1\sin\beta - 2u_{2n}\right). \end{aligned}\right\} \tag{C3}$$

In general, there are two branches of oblique shock solutions, namely the strong and the weak oblique shock solutions. To ensure that the iteration process converges to the different solution branches of OSWs exactly, different iteration initial values are used as follows:

$$\beta_0 = \begin{cases} \max(\arcsin Ma_1^{-1}, \theta) + 0.1^\circ & \text{for a weak oblique shock,} \\ 89.9^\circ & \text{for a strong oblique shock,} \end{cases} \tag{C4}$$

where Ma_1 is the Mach number before the oblique shock. After β is known, other unknown post-shock parameters can be obtained directly by substituting β into the oblique shock governing equations.

Appendix D. Calculation of the isentropic relationship with varying compositions

Problem description: the pressure p_1, temperature T_1, velocity u_1 and chemical compositions x_{i1} (moles of species per unit mass of the mixture) before starting an isentropic process are known. Notably, the mixture must be in chemical equilibrium before starting an isentropic process with varying compositions. Additionally, the chemical compositions x_{i2} (they also do not need to be the same as x_{i1} to account for shifts in chemical equilibrium during the isentropic process) and the pressure p_2 after the isentropic process are known. Then, the temperature T_2 and velocity u_2 after the isentropic process are solved. A single-variable Newton iteration method is employed again, which is directly derived from the isentropic condition of the mixture. The iteration variable is the temperature T_2, and the iteration function $f_{isen}(T_2)$ is expressed as

$$\begin{aligned} f_{isen}(T_2) = &\sum_{i=1}^{nSp}[x_{i2}S_i^0(T_2)] - \sum_{i=1}^{nSp}[x_{i1}S_i^0(T_1)] - R_u\ln p_2\sum_{i=1}^{nSp}x_{i2} + R_u\ln p_1\sum_{i=1}^{nSp}x_{i1} \\ &+ R_u\left[\ln p_{\mathrm{atm}}\sum_{i=1}^{nSp}x_{i2} - \sum_{i=1}^{nSp}(x_{i2}\ln x_{i2})\right] - R_u\left[\ln p_{\mathrm{atm}}\sum_{i=1}^{nSp}x_{i1} - \sum_{i=1}^{nSp}(x_{i1}\ln x_{i1})\right] = 0, \end{aligned} \tag{D1}$$

where $S_i^0(T)$ is the species standard molar entropy at temperature T and can also be obtained from a species thermodynamic database; $R_u = 8.314\ \mathrm{J\ mol^{-1}\ K^{-1}}$ is the universal gas constant; and $p_{atm} = 1.01325 \times 10^5$ Pa is the pressure value defined under standard conditions. The Newton iteration formula appears as

$$T_{2,k+1} = T_{2,k} - \frac{f_{isen}(T_{2,k})}{f'_{isen}(T_{2,k})}, \tag{D2}$$

with the derivative of the iteration function, $f'_{isen}(T_2)$, given by

$$f'_{isen}(T_2) = \sum_{i=1}^{nSp}\left[x_i \frac{\mathrm{d}S_i^0(T_2)}{\mathrm{d}T_2}\right] = \sum_{i=1}^{nSp}\left[x_i \frac{1}{T_2} C_{pi}^0(T_2)\right]. \tag{D3}$$

In (D3), $C_{pi}^0(T)$ is the species constant-pressure molar heat capacity at temperature T. After T_2 is known, u_2 can be obtained directly through the energy conservation equation. Furthermore, if an area ratio of the isentropic process is needed, it can be obtained easily by substituting p_2, T_2 and u_2 into the equation of state of the mixture and the mass conservation equation.

Appendix E. Calculation of chemical equilibrium compositions at a specific temperature and pressure

Problem description: the initial compositions of the mixture are known, i.e. the total moles of atoms of element j, b_j ($j = 1, \ldots, nEl$, where nEl is the number of elements involved in the mixture), and the number of atoms of element j in species i, a_{ij}, are known. Then, the equilibrium compositions at a specific temperature T and pressure p are solved. The minimization of free energy method of NASA (Gordon & Mcbride 1994) is used. Let y_i (moles of species per unit mass of the mixture) be an estimate of the equilibrium compositions; then, the new estimate x_i can be evaluated by

$$x_i = -d_i + y_i\left(\frac{\sum x_i}{\sum y_i} + \sum_{j=1}^{nEl}\lambda_j a_{ij}\right), \quad \text{for } i = 1 \ldots nSp, \tag{E1}$$

where d_i is defined as

$$d_i \equiv y_i\left(\frac{G_i^0}{RT} + \ln\frac{y_i}{\sum y_i} + \ln p\right), \quad \text{for } i = 1 \ldots nSp. \tag{E2}$$

In (E2), G_i^0 is the species standard molar Gibbs free energy. Moreover, the unknowns $\sum x_i / \sum y_i$ and λ_j in (E1) are the solutions of the following linear equations:

$$\left.\begin{aligned} \sum_{j=1}^{nEl}\lambda_j \sum_{i=1}^{nSp} y_i a_{ij} &= \sum_{i=1}^{nSp} d_i, \\ \sum_{i=1}^{nSp}(-a_{ij}d_i) + \frac{\sum x_i}{\sum y_i}\sum_{i=1}^{nSp} y_i a_{ij} + \sum_{k=1}^{nEl}\lambda_k \sum_{i=1}^{nSp} a_{ik}a_{ij}y_i - b_j &= 0, \quad \text{for } j = 1, \ldots, nEl. \end{aligned}\right\} \tag{E3}$$

After x_i has been solved, it serves as the new y_i in an iterative process until convergence is achieved.

References

Alexander, D.C. & Sislian, J.P. 2008 Computational study of the propulsive characteristics of a shcramjet engine. *J. Propul. Power* **24** (1), 34–44.

Alexander, D.C., Sislian, J.P. & Parent, B. 2006 Hypervelocity fuel/air mixing in mixed-compression inlets of shcramjets. *AIAA J.* **44** (10), 2145–2155.

Ben-Dor, G. 2007 *Shock Wave Reflection Phenomena*, 2nd edn. Springer.

Cai, X., Deiterding, R., Liang, J. & Mahmoudi, Y. 2017 Adaptive simulations of viscous detonations initiated by a hot jet using a high-order hybrid WENO-CD scheme. *Proc. Combust. Inst.* **36** (2), 2725–2733.

Cai, X., Deiterding, R., Liang, J., Mahmoudi, Y. & Sun, M. 2021 Mechanism of detonation stabilization in a supersonic model combustor. *J. Fluid Mech.* **910**, A40.

Cai, X., Deiterding, R., Liang, J., Sun, M. & Dong, D. 2019 Dynamic detonation stabilization in supersonic expanding channels. *Phys. Rev. Fluids* **4**, 083201.

Cai, X., Deiterding, R., Liang, J., Sun, M. & Dong, D. 2020 Detonation stabilization in supersonic flow: effects of suction boundaries. *AIAA J.* **58** (3), 1348–1355.

Cai, X., Deiterding, R., Liang, J., Sun, M. & Mahmoudi, Y. 2018*a* Diffusion and mixing effects in hot jet initiation and propagation of hydrogen detonations. *J. Fluid Mech.* **836**, 324–351.

Cai, X., Liang, J., Deiterding, R. & Lin, Z. 2016 Adaptive simulations of cavity-based detonation in supersonic hydrogen-oxygen mixture. *Intl J. Hydrogen Energy* **41** (16), 6917–6928.

Cai, X., Liang, J., Deiterding, R., Mahmoudi, Y. & Sun, M. 2018*b* Experimental and numerical investigations on propagating modes of detonations: detonation wave/boundary layer interaction. *Combust. Flame* **190**, 201–215.

Chakravarthy, S. 1999 A unified-grid finite volume formulation for computational fluid dynamics. *Intl J. Numer. Meth. Fluids* **31** (1), 309–323.

Chang, J., Li, N., Xu, K., Bao, W. & Yu, D. 2017 Recent research progress on unstart mechanism, detection and control of hypersonic inlet. *Prog. Aerosp. Sci.* **89**, 1–22.

Chapuis, M., Fedina, E., Fureby, C., Hannemann, K., Karl, S. & Schramm, J.M. 2013 A computational study of the HyShot II combustor performance. *Proc. Combust. Inst.* **34** (2), 2101–2109.

Choi, J.Y., Jeung, I.S. & Yoon, Y. 2000 Computational fluid dynamics algorithms for unsteady shock-induced combustion, part 1: validation. *AIAA J.* **38** (7), 1179–1187.

Choi, J.Y., Kim, D.W., Jeung, I.S., Ma, F. & Yang, V. 2007 Cell-like structure of unstable oblique detonation wave from high-resolution numerical simulation. *Proc. Combust. Inst.* **31** (2), 2473–2480.

Choi, J.Y., Shin, E.J.R. & Jeung, I.S. 2009 Unsteady combustion induced by oblique shock waves at the non-attaching condition of the oblique detonation wave. *Proc. Combust. Inst.* **32** (2), 2387–2396.

Curran, E.T. & Murthy, S.N.B. 2001 *Scramjet Propulsion*. American Institute of Aeronautics and Astronautics.

Ess, P.R., Sislian, J.P. & Allen, C.B. 2005 Blunt-body generated detonation in viscous hypersonic ducted flows. *J. Propul. Power* **21** (4), 667–680.

Fang, Y., Zhang, Z., Hu, Z. & Deng, X. 2019 Initiation of oblique detonation waves induced by a blunt wedge in stoichiometric hydrogen-air mixtures. *Aerosp. Sci. Technol.* **92**, 676–684.

Fureby, C., Chapuis, M., Fedina, E. & Karl, S. 2011 CFD analysis of the HyShot II scramjet combustor. *Proc. Combust. Inst.* **33** (2), 2399–2405.

Gordon, S. & Mcbride, B.J. 1994 Computer program for calculation of complex chemical equilibrium compositions and applications: I. Analysis. NASA Reference Publication 1311.

Grossman, I.J. & Bruce, P.J.K. 2018 Confinement effects on regular-irregular transition in shock-wave–boundary-layer interactions. *J. Fluid Mech.* **853**, 171–204.

Han, X. 2013 Research on detonation initiation and propagation mechanisms in supersonic premixed flows. PhD thesis, National University of Defense Technology.

Han, W., Wang, C. & Law, C.K. 2019 Three-dimensional simulation of oblique detonation waves attached to cone. *Phys. Rev. Fluids* **4**, 053201.

Higgins, A.J. 1997 The effect of confinement on detonation initiation by blunt projectiles. *AIAA Paper* 97-3179.

Higgins, A.J. 2006 Ram accelerators: outstanding issues and new directions. *J. Propul. Power* **22** (6), 1170–1187.

Higgins, A.J., Knowlen, C. & Bruckner, A.P. 1998 Ram accelerator operating limits, part 2: nature of observed limits. *J. Propul. Power* **14** (6), 959–966.

Im, S.K. & Do, H. 2018 Unstart phenomena induced by flow choking in scramjet inlet-isolators. *Prog. Aerosp. Sci.* **97**, 1–21.

Jachimowski, C.J. 1988 An analytical study of the hydrogen-air reaction mechanism with application to scramjet combustion. *NASA Technical Paper* 2791.

JIANG, Z., ZHANG, Z., LIU, Y., WANG, C. & LUO, C. 2021 Criteria for hypersonic airbreathing propulsion and its experimental verification. *Chin. J. Aeronaut.* **34** (3), 94–104.

KAILASANATH, K. 2000 Review of propulsion applications of detonation waves. *AIAA J.* **38**, 1698–1708.

KNOWLEN, C., HIGGINS, A.J., BRUCKNER, A.P. & HERTZBERG, A. 1995 In-tube photography of ram accelerator projectiles. In *Proceedings of the 19th International Symposium on Shock Waves*, pp. 617–622. Springer-Verlag.

LI, H. & BEN-DOR, G. 1997 A parametric study of Mach reflection in steady flows. *J. Fluid Mech.* **341**, 101–125.

LI, C., KAILASANATH, K. & ORAN, E.S. 1994 Detonation structures behind oblique shocks. *Phy. Fluids* **6**, 1600–1611.

LIN, Z., ZHANG, J. & ZHOU, J. 2007 Design of high-enthalpy premixed supersonic heater and experimental study of detonation. *AIAA Paper* 2007-5009.

LU, F.K. & BRAUN, E.M. 2014 Rotating detonation wave propulsion: experimental challenges, modeling, and engine concepts. *J. Propul. Power* **30** (5), 1125–1142.

LU, F.K., FAN, H. & WILSON, D.R. 2006 Detonation waves induced by a confined wedge. *Aerosp. Sci. Technol.* **10** (8), 679–685.

MA, J.Z., LUAN, M.Y., XIA, Z.J., WANG, J.P., ZHANG, S.J., YAO, S.B. & WANG, B. 2020 Recent progress, development trends, and consideration of continuous detonation engines. *AIAA J.* **58** (12), 4976–5035.

MAEDA, S., KASAHARA, J. & MATSUO, A. 2012 Oblique detonation wave stability around a spherical projectile by a high time resolution optical observation. *Combust. Flame* **159** (2), 887–896.

MAEDA, S., SUMIYA, S., KASAHARA, J. & MATSUO, A. 2013 Initiation and sustaining mechanisms of stabilized oblique detonation waves around projectiles. *Proc. Combust. Inst.* **34** (2), 1973–1980.

MATHEIS, J. & HICKEL, S. 2015 On the transition between regular and irregular shock patterns of shock-wave/boundary layer interactions. *J. Fluid Mech.* **776**, 200–234.

MCBRIDE, B.J., GORDON, S. & RENO, M.A. 1993 Coefficients for calculating thermodynamic and transport properties of individual species. *NASA Technical Memorandum* 4513.

MIAO, S., XU, D., SONG, T. & YU, J. 2020 Shock wave–boundary layer interactions in wedge-induced oblique detonations. *Combust. Sci. Technol.* **192** (12), 2345–2370.

MIAO, S., ZHOU, J., LIU, S. & CAI, X. 2018 Formation mechanisms and characteristics of transition patterns in oblique detonations. *Acta Astronaut.* **142**, 121–129.

MOUTON, C.A. & HORNUNG, H.G. 2007 Mach stem height and growth rate predictions. *AIAA J.* **45** (8), 1977–1987.

QIN, Q. & ZHANG, X. 2018 A novel method for trigger location control of the oblique detonation wave by a modified wedge. *Combust. Flame* **197**, 65–77.

REN, Z., WANG, B., XIANG, G. & ZHENG, L. 2018 Effect of the multiphase composition in a premixed fuel-air stream on wedge-induced oblique detonation stabilization. *J. Fluid Mech.* **846**, 411–427.

REN, Z., WANG, B., XIANG, G. & ZHENG, L. 2019 Numerical analysis of wedge-induced oblique detonations in two-phase kerosene-air mixtures. *Proc. Combust. Inst.* **37** (3), 3627–3635.

REN, Z., WANG, B. & ZHENG, L. 2021 Wedge-induced oblique detonation waves in supersonic kerosene-air premixing flows with oscillating pressure. *Aerosp. Sci. Technol.* **110**, 106472.

ROPP, D.L. & SHADID, J.N. 2009 Stability of operator splitting methods for systems with indefinite operators: advection-diffusion-reaction systems. *J. Comput. Phys.* **228** (9), 3508–3516.

ROY, G.D., FROLOV, S.M., BORISOV, A.A. & NETZER, D.W. 2004 Pulse detonation propulsion: challenges, current status, and future perspective. *Prog. Energy Combust. Sci.* **30** (6), 545–672.

SCHWARTZENTRUBER, T.E., SISLIAN, J.P. & PARENT, B. 2005 Suppression of premature ignition in the premixed inlet flow of a shcramjet. *J. Propul. Power* **21** (1), 87–94.

SEILER, F., PATZ, G., SMEETS, G. & SRULIJES, J. 1998 Influence of projectile material and gas composition on superdetonative combustion in ISL's RAMAC30. *AIAA Paper* 98-3445.

SEILER, F., PATZ, G., SMEETS, G. & SRULIJES, J. 2000 Progress of ram acceleration with ISL's RAMAC30. *J. Phys.* IV **10**, Pr11-31–Pr11-40.

SELEZNEV, R.K., SURZHIKOV, S.T. & SHANG, J.S. 2019 A review of the scramjet experimental data base. *Prog. Aerosp. Sci.* **106**, 43–70.

SHEN, H. & PARSANI, M. 2017 The role of multidimensional instabilities in direct initiation of gaseous detonations in free space. *J. Fluid Mech.* **813**, R4.

SHI, L., SHEN, H., ZHANG, P., ZHANG, D. & WEN, C. 2017 Assessment of vibrational non-equilibrium effect on detonation cell size. *Combust. Sci. Technol.* **189** (5), 841–853.

SHI, L., UY, K.C.K. & WEN, C.Y. 2020 The re-initiation mechanism of detonation diffraction in a weakly unstable gaseous mixture. *J. Fluid Mech.* **895**, A24.

STERLING, J.D., CUMMINGS, E.B., GHORBANIAN, K., PRATT, D.T., SOBOTA, T.H., BROCK, N.J., BROWN, M.S., SEGALL, J. & DEBARBER, P. 1998 Oblique detonation wave studies in the Caltech T-5 shock tunnel facility. *AIAA*-98-1561.

TAO, Y., FAN, X. & ZHAO, Y. 2014 Viscous effects of shock reflection hysteresis in steady supersonic flows. *J. Fluid Mech.* **759**, 134–148.

TENG, H.H. & JIANG, Z.L. 2012 On the transition pattern of the oblique detonation structure. *J. Fluid Mech.* **713**, 659–669.

TENG, H.H., JIANG, Z.L. & NG, H.D. 2014 Numerical study on unstable surface of oblique detonations. *J. Fluid Mech.* **744**, 111–128.

TENG, H., LIU, S. & ZHANG, Z. 2020 Unsteady combustion mode with a super-high frequency induced by a curved shock. *Phy. Fluids* **32**, 116101.

TENG, H., NG, H.D. & JIANG, Z. 2017 Initiation characteristics of wedge-induced oblique detonation waves in a stoichiometric hydrogen-air mixture. *Proc. Combust. Inst.* **36**, 2735–2742.

TENG, H., TIAN, C., ZHANG, Y., ZHOU, L. & NG, H.D. 2021 Morphology of oblique detonation waves in a stoichiometric hydrogen-air mixture. *J. Fluid Mech.* **913**, A1.

TORO, E.F. 2013 *Riemann Solvers and Numerical Methods for Fluid Dynamics: A Practical Introduction*. Springer Science & Business Media.

URZAY, J. 2018 Supersonic combustion in air-breathing propulsion systems for hypersonic flight. *Annu. Rev. Fluid Mech.* **50**, 593–627.

UY, K.C.K., SHI, L., HAO, J. & WEN, C.Y. 2020 Linear stability analysis of one-dimensional detonation coupled with vibrational relaxation. *Phy. Fluids* **32**, 126101.

VERREAULT, J. & HIGGINS, A.J. 2011 Initiation of detonation by conical projectiles. *Proc. Combust. Inst.* **33** (2), 2311–2318.

VIGUIER, C., DA SILVA, L.F.F., DESBORDES, D. & DESHAIES, B. 1996 Onset of oblique detonation waves: comparison between experimental and numerical results for hydrogen-air mixtures. *Symp. (Intl) Combust.* **26** (2), 3023–3031.

WANG, Y.W. & SISLIAN, J.P. 2010 Numerical simulation of gaseous hydrocarbon fuel injection in a hypersonic inlet. *J. Propul. Power* **26** (5), 1114–1124.

WANG, K., TENG, H., YANG, P. & NG, H.D. 2020*a* Numerical investigation of flow structures resulting from the interaction between an oblique detonation wave and an upper expansion corner. *J. Fluid Mech.* **903**, A28.

WANG, K., YANG, P. & TENG, H. 2021 Steadiness of wave complex induced by oblique detonation wave reflection before an expansion corner. *Aerosp. Sci. Technol.* **112**, 106592.

WANG, K., ZHANG, Z., YANG, P. & TENG, H. 2020*b* Numerical study on reflection of an oblique detonation wave on an outward turning wall. *Phy. Fluids* **32**, 046101.

WILSON, G.J. & MACCORMACK, R.W. 1992 Modeling supersonic combustion using a fully implicit numerical-method. *AIAA J.* **30** (4), 1008–1015.

WOLAŃSKI, P. 2013 Detonative propulsion. *Proc. Combust. Inst.* **34**, 125–158.

XIANG, G., LI, X., SUN, X. & CHEN, X. 2019 Investigations on oblique detonations induced by a finite wedge in high altitude. *Aerosp. Sci. Technol.* **95**, 105451.

XIANG, G., LI, H., ZHANG, G., XIE, X. & ZHANG, Y. 2021*a* Characteristics of the oblique detonation flow field induced by a complex wave structure. *Intl J. Hydrogen Energy* **46** (33), 17435–17445.

XIANG, G., ZHANG, Y., GAO, X., LI, H. & HUANG, X. 2021*b* Oblique detonation waves induced by two symmetrical wedges in hydrogen-air mixtures. *Fuel* **295**, 120615.

XUE, L., WANG, C. & CHENG, K. 2021 A study on the RR-to-MR transition of shock wave reflections near the leading edge in hypersonic flows. *J. Fluid Mech.* **919**, A40.

YANG, P., NG, H.D. & TENG, H. 2019*a* Numerical study of wedge-induced oblique detonations in unsteady flow. *J. Fluid Mech.* **876**, 264–287.

YANG, P., NG, H.D. & TENG, H. 2021 Unsteady dynamics of wedge-induced oblique detonations under periodic inflows. *Phy. Fluids* **33**, 016107.

YANG, P., TENG, H., NG, H.D. & JIANG, Z. 2019*b* A numerical study on the instability of oblique detonation waves with a two-step induction-reaction kinetic model. *Proc. Combust. Inst.* **37** (3), 3537–3544.

YATSUFUSA, T. & TAKI, S. 2002 Visualization of burning flow around a ram accelerator projectile by coaxial simultaneous shadow/direct photography. *Shock Waves* **12** (3), 235–240.

ZHANG, Z. 2020*a* Oblique detonation propulsion theory, technology and its experimental demonstration. PhD thesis, University of Chinese Academy of Sciences.

ZHANG, Y., FANG, Y., NG, H.D. & TENG, H. 2019 Numerical investigation on the initiation of oblique detonation waves in stoichiometric acetylene-oxygen mixtures with high argon dilution. *Combust. Flame* **204**, 391–396.

ZHANG, Z., MA, K., ZHANG, W., HAN, X., LIU, Y. & JIANG, Z. 2020*b* Numerical investigation of a Mach 9 oblique detonation engine with fuel pre-injection. *Aerosp. Sci. Technol.* **105**, 106054.

ZHANG, B., MEHRJOO, N., NG, H.D., LEE, J.H.S. & BAI, C. 2014 On the dynamic detonation parameters in acetylene-oxygen mixtures with varying amount of argon dilution. *Combust. Flame* **161**, 1390–1397.

ZHANG, B., NG, H.D. & LEE, J.H.S. 2012 The critical tube diameter and critical energy for direct initiation of detonation in $C_2H_2/N_2O/Ar$ mixtures. *Combust. Flame* **159**, 2944–2953.

ZHANG, Z., WEN, C., YUAN, C., LIU, Y., HAN, G., WANG, C. & JIANG, Z. 2022 An experimental study of formation of stabilized oblique detonation waves in a combustor. *Combust. Flame* **237**, 111868.

ZHANG, Z., WEN, C., ZHANG, W., LIU, Y. & JIANG, Z. 2021*a* A theoretical method for solving shock relations coupled with chemical equilibrium and its applications. *Chin. J. Aeronaut*. https://doi.org/10.1016/j.cja.2021.08.021.

ZHANG, Z., WEN, C., ZHANG, W., LIU, Y. & JIANG, Z. 2021*b* Formation of stabilized oblique detonation waves in a combustor. *Combust. Flame* **223**, 423–436.